J. Fluid Mech. (2003), *vol.* 492, *pp.* 381–410.
DOI: 10.1017/S0022112003005688 Printed in the United Kingdom

Instabilities of granular material undergoing vertical vibrations: a uniformly driven layer

By RENSHENG DENG[1] AND CHI-HWA WANG[1,2]†

[1]Singapore-MIT Alliance, 4 Engineering Drive 3, Singapore, 117576

[2]Department of Chemical & Environmental Engineering, National University of Singapore, 4 Engineering Drive 4, Singapore, 117576

(Received 29 July 2002 and in revised form 27 May 2003)

In this paper, the stability of a uniformly driven granular layer is examined by linear stability analysis. This includes two main steps: first the base state at various values of mass holdup (M_t) and energy input (Q_t) is calculated; and, secondly, small perturbations are introduced to verify the stability of the base state by solving the linearized governing equations and corresponding boundary conditions. Results from the base-state solution show that, for a given pair of M_t and Q_t, solid fraction tends to increase at first up the layer height and then decrease after a certain vertical position. In contrast, granular temperature decreases rapidly from the bottom plate to the top surface. The stability diagram is constructed by checking the eigenvalues at different points in the (M_t, Q_t) plane, and their dependence on the operating conditions and materials properties is also investigated. For the unstable regime, pattern formation is illustrated with the variation of solid fraction with vertical position. For the layer mode, there are no variations at different horizontal positions. In contrast, a periodic feature is found for the stationary mode in which alternating particle clusters and voids are observed in the horizontal direction. By introducing perturbations in different directions, we have produced surface patterns such as stripes, squares and hexagons. Besides the solid fraction distribution, other variables such as the profiles of velocities and granular temperatures are also examined.

1. Introduction

Granular material undergoing vertical vibration is of interest to engineers and scientists for both practical and theoretical reasons. For instance, shakers are widely used in mixing, separation and particle drying processes, commonly seen in industries such as mining, agriculture, pharmacy and construction. The occurrence of complex behaviours in the assembly, such as the formation of travelling waves (Pak & Behringer 1993) and standing waves (Umbanhowar 1997) on the free surface, has provided an exciting challenge to fundamental research in powder technology.

Various planar patterns like stripes, squares and hexagons, together with local structures like spirals and oscillons have recently been investigated in experiments (Melo, Umbanhowar & Swinney 1994, 1995; Umbanhowar, Melo & Swineey 1996, 1998; Umbanhowar & Swinney 2000; Metcalf, Knight & Jaeger 1997; Clement *et al.* 1996), and possible mechanisms have also been proposed to explain the instabilities

† Author to whom correspondence should be addressed: chewch@nus.edu.sg

that appear (Aoki & Akiyama 1996; Luding *et al.* 1994; Tsimring & Aranson 1997; Shinbrot 1997; Bizon *et al.* 1998*a*, 1999). Bizon *et al.* (1998*b*) applied discrete particle simulations to the study of convection and diffusion in this system and the results obtained compared well with experiments. However, most of the work concentrates on the surface patterns, and further theoretical/simulation models are necessary to explain the findings from experiments in all aspects of these systems.

A stability analysis method based on the grain kinetic theory has been successfully applied to study the instabilities occurring in granular flow systems (Wang, Sundaresan & Jackson 1997; Wang & Tong 2001). In the application of hydrodynamic equations to granular flows, Kadanoff (1999) found that some behaviours in the one-dimensional system could not be predicted by any hydrodynamic type of analysis while hydrodynamics seems to work very well for the two-dimensional system. Although it had been argued that a continuum model is not always successful for all granular flows, Shattuck *et al.* (1999) proved that in a certain case (e.g. vertically vibrated layer) the results from kinetic theory agree remarkably well with those from event-driven molecular dynamics simulations.

In this paper, the method mentioned above is used to examine the instabilities appearing in granular material undergoing vertical vibrations. A base-state solution is first found by solving the macroscopic balance equations based on the grain kinetic theory, and secondly, small perturbations are introduced to examine the stability of the corresponding base state and the resultant new patterns that may develop.

2. Governing equations

Figure 1 shows the case to be studied. A bed (height H_0, mass holdup m_p) of granular material (particle density ρ_p, particle diameter d_p) is placed on top of a vertically vibrated flat plate. Here mass holdup is defined as the mass of particles per unit area of the bottom plate. This process is simplified by taking an average over one period of particle movement, thus the energy flux supplied from the bottom plate to the granular layers can be viewed as constant (denoted by Q_0), and the bed expands from its original height to H. Note that such an averaging method turns the vibrated bed problem into a uniformly driven layer, thus the following stability analysis will be for this situation only. In the base state, the free surface of the granular materials is flat. The zero point of the y-axis is set at the centreline of the vibrating bottom plate, and x and z are assumed to be infinite because the shape and size of the container do not influence the stability of the system when the dimension of container is much greater than the particle size (Melo *et al.* 1994). The 'flow field' is considered as steady, and the mean velocity of particles in all directions is zero. Furthermore, the friction between particles is neglected and only inelastic collisions are considered during particle–particle and particle–wall contact.

The conservation equations of mass, momentum and pseudo-thermal energy are those used by Johnson & Jackson (1987), Wang *et al.* (1997) and Wang & Tong (1998, 2001):

$$\text{continuity:} \qquad \frac{\partial \rho}{\partial t} + \nabla \cdot (\rho \boldsymbol{u}) = 0, \tag{1}$$

$$\text{momentum:} \qquad \rho \frac{\mathrm{D}\boldsymbol{u}}{\mathrm{D}t} = -\rho \boldsymbol{g} - \nabla \cdot \boldsymbol{\sigma}, \tag{2}$$

$$\text{energy:} \qquad \frac{3}{2}\rho \frac{\mathrm{D}T}{\mathrm{D}t} = -\nabla \cdot \boldsymbol{q} - \boldsymbol{\sigma} : \nabla \boldsymbol{u} - J. \tag{3}$$

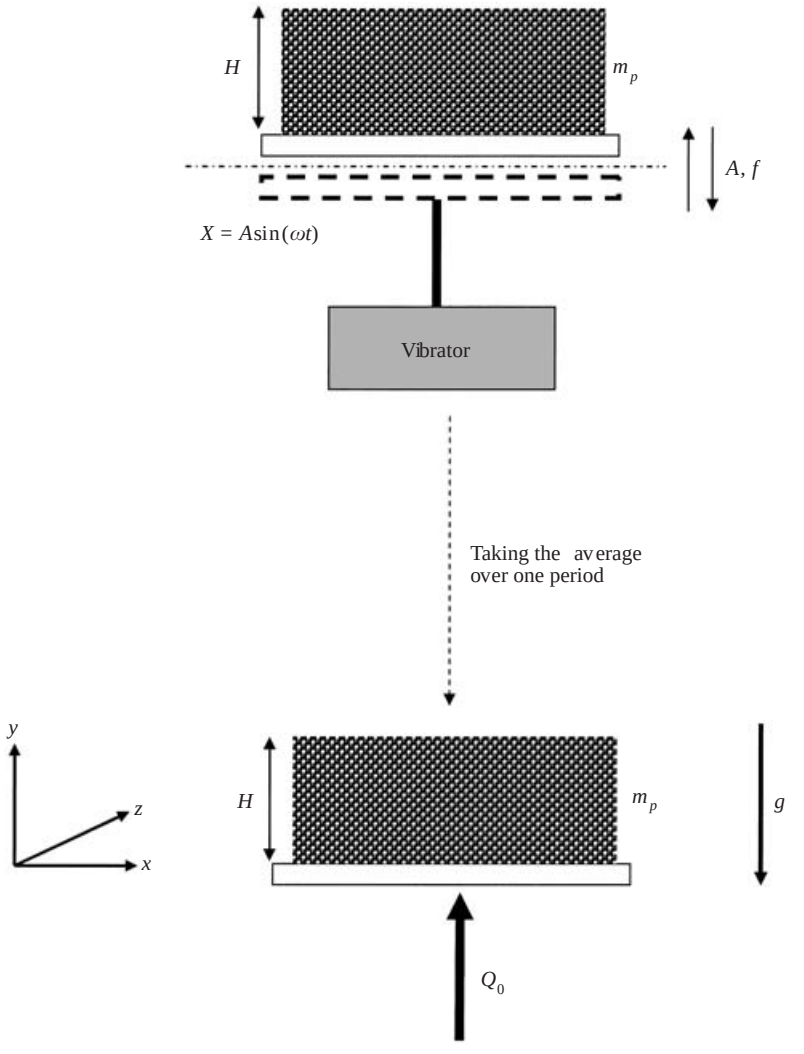

FIGURE 1. Granular material under vertical vibrations. A and f are the vibration acceleration and frequency, respectively. g is the gravitational acceleration.

Here $\boldsymbol{g}$ is the gravity force; ρ is the bulk density of the material, given by $\rho = \rho_p \nu$, where ν is the volume fraction of solids; $\boldsymbol{u}$ is the local mean velocity; $\boldsymbol{\sigma}$ is the stress tensor for the granular assembly; T is the granular temperature, defined as $(1/3)\langle \boldsymbol{u}'^2 \rangle$, where $\boldsymbol{u}'$ is the magnitude of the fluctuation about the local mean velocity; $\boldsymbol{q}$ is the flux vector of the pseudo-thermal energy associated with the fluctuations in particle velocity; and J denotes the rate of dissipation of this energy, per unit volume, by inelastic collisions between particles. $\mathrm{D}/\mathrm{D}t$ represents the material time derivative following the mean motion.

The constitutive relationships for $\boldsymbol{\sigma}$, $\boldsymbol{q}$ and J are those of Lun *et al.* (1984), namely

$$\boldsymbol{\sigma} = [\rho T(1 + 4\eta\nu g_0) - \eta\mu_b \nabla \cdot \boldsymbol{u}]\boldsymbol{I} - \left(\frac{2+\alpha}{3}\right)\left\{\frac{2\mu}{\eta(2-\eta)g_0}\left(1 + \tfrac{8}{5}\eta\nu g_0\right)\left[1 + \tfrac{8}{5}\eta(3\eta - 2)\nu g_0\right] + \tfrac{6}{5}\mu_b\eta\right\}\boldsymbol{S}, \quad (4)$$

Particle diameter, d_p (m)	0.0005
Solid material density, ρ_p (kg/m^3)	2500
Particle-particle coefficient of restitution, e_p	0.9
Particle-wall coefficient of restitution, e_w	0.5
Specularity coefficient for wall collision, ϕ'	0.6
Parameter, α, in equation (4)	1.6

TABLE 1. Parameters used in the simulation.

$$\boldsymbol{q} = -\frac{\lambda}{g_0}\left\{\left(1+\tfrac{12}{5}\eta\nu g_0\right)\left[1+\tfrac{12}{5}\eta^2(4\eta-3)\nu g_0\right]+\frac{64}{25\pi}(41-33\eta)(\eta\nu g_0)^2\right\}\nabla T$$

$$-\frac{\lambda}{g_0}\tfrac{12}{5}\eta(\eta-1)(2\eta-1)\left(1+\tfrac{12}{5}\eta\nu g_0\right)\frac{\mathrm{d}}{\mathrm{d}\nu}(\nu^2 g_0)\frac{T}{\nu}\nabla\nu, \quad (5)$$

$$J = \frac{48}{\pi^{0.5}}\eta(1-\eta)\frac{\rho_P\nu^2}{d_P}g_0T^{1.5}, \quad (6)$$

where $\boldsymbol{S}$ is the deviatoric part of the rate of deformation:

$$\boldsymbol{S} = \tfrac{1}{2}(\nabla\boldsymbol{u}+\nabla\boldsymbol{u}^T)-\tfrac{1}{3}(\nabla\cdot\boldsymbol{u})\boldsymbol{I},$$

and η is related to e_p, the coefficient of restitution for the collisions between particles:

$$\eta = \tfrac{1}{2}(1+e_P).$$

The two viscosity factors μ and μ_b, and the thermal conductivity coefficient λ, are given by

$$\mu = \frac{5M(T/\pi)^{0.5}}{16d_P^2}, \quad \mu_b = \frac{256\mu\nu^2 g_0}{5\pi}, \quad \lambda = \frac{75M(T/\pi)^{0.5}}{8\eta(41-33\eta)d_P^2},$$

where M and d_p are the mass and diameter of a particle, respectively. For g_0 we adopt the form used by Johnson & Jackson (1987), namely

$$g_0(\nu) = \frac{1}{1-(\nu/\nu_m)^{1/3}}$$

where ν_m is the solids volume fraction at closest packing, taken to be 0.65. Except for special cases indicated, the values of ρ_p, d_p and other parameters used in the present simulation are given in table 1.

Boundary conditions at the bottom plate, which take account of momentum and energy transfer between the wall and the materials, are the same as those used by Johnson & Jackson (1987),

$$\boldsymbol{t}\cdot\boldsymbol{\sigma}\cdot\boldsymbol{n}+\left(\frac{\pi\sqrt{3}}{6\nu_m}\right)\phi'\rho_P\nu g_0(\nu)T^{1/2}u_{sl}=0, \quad (7)$$

$$\boldsymbol{n}\cdot\boldsymbol{q} = \left(\frac{\pi\sqrt{3}}{6\nu_m}\right)\phi'\rho_P\nu g_0(\nu)T^{1/2}u_{sl}^2+Q_0-\left(\frac{\pi\sqrt{3}}{4\nu_m}\right)\left(1-e_w^2\right)\rho_P\nu g_0(\nu)T^{3/2}. \quad (8)$$

In equations (7) and (8), $\boldsymbol{n}$ is the unit normal to the wall, pointing into the granular material, u_{sl} is the velocity of the granular material in contact with the wall, and $\boldsymbol{t}$ is a unit vector tangent to the wall, in the direction of the slip velocity. The nature of

the plate is characterized by ϕ', a specularity factor (which measures the fraction of the momentum of an incident particle in the direction of slip which is transmitted, on average, to the wall in a collision), and e_w, is the coefficient of restitution for collisions between particles and the wall. Since the value of u_{sl} is zero for the base state, equation (7) is satisfied trivially.

One boundary condition at the free surface can be obtained by examining the force balance for particles in the top layer, that is, gravity should be balanced by the supporting force from the material

$$M\boldsymbol{g} = (\boldsymbol{n}\cdot\boldsymbol{\sigma})a_c, \tag{9a}$$

where a_c is the effective area occupied by a particle

$$a_c = d_P^2\left(\frac{\nu_m}{\nu}\right)^{2/3}. \tag{9b}$$

Another boundary condition is obtained from the fact that there is no energy input at the free surface, thus

$$\boldsymbol{n}\cdot\boldsymbol{q} = 0. \tag{10}$$

Dimensionless variables are introduced as follows:

$$(X, Y, Z) = \frac{(x, y, z)}{H}, \quad (U^*, V^*, W^*) = \frac{(U, V, W)}{\sqrt{gH}}, \quad T^* = \frac{T}{gd_p}, \quad \tau = \frac{t}{\sqrt{H/g}}, \tag{11}$$

and

$$M_t = \frac{m_P}{\rho_P d_P}, \quad Q_t = \frac{Q_0}{\rho_P(d_P g)^{3/2}}. \tag{12}$$

After substitution and non-dimensionlization, the base-state equations have the following form:

$$\frac{1}{C}\int_Y^1 \nu\,\mathrm{d}Y = f_1(\nu)T^* - \frac{\pi}{6}\left(\frac{\nu}{\nu_m}\right)^{2/3}, \tag{13}$$

$$\frac{\partial}{\partial Y}\left[f_3(\nu)T^{*1/2}\frac{\mathrm{d}T^*}{\mathrm{d}Y} + f_4(\nu)T^{*3/2}\frac{\mathrm{d}\nu}{\mathrm{d}Y}\right] - \frac{1}{C^2}f_5(\nu)T^{*3/2} = 0, \tag{14}$$

together with the boundary conditions

$$\mathrm{Y} = 0: \quad f_3(\nu)T^{*1/2}\frac{\mathrm{d}T^*}{\mathrm{d}Y} + f_4(\nu)T^{*3/2}\frac{\mathrm{d}\nu}{\mathrm{d}Y} = \frac{(1-e_w^2)f_3(\nu)f_6(\nu)T^{*3/2}}{C} - \frac{Q_0}{C\rho_P g^{3/2}d_P^{3/2}}, \tag{15}$$

$$\mathrm{Y} = 1: \quad f_3(\nu)T^{*1/2}\frac{\mathrm{d}T^*}{\mathrm{d}Y} + f_4(\nu)T^{*3/2}\frac{\mathrm{d}\nu}{\mathrm{d}Y} = 0, \tag{16}$$

where the dimensionless group C is given by

$$C = d_P/H. \tag{17}$$

The dimensionless functions f_1-f_9 (some are used in the stability analysis) are listed in table 2.

A finite difference method is used here to solve the above equations. The interval of [0,1] on the Y-axis is divided into 100 sub-intervals, and both the equations and boundary conditions are discretized at the grid points. Given the values of M_t and

$$f_1(\nu) = \nu[1 + 4\eta\nu g_0(\nu)]$$

$$f_2(\nu) = \frac{(2+\alpha)5\pi^{1/2}}{288\eta(2-\eta)}\left[\frac{1}{g_0(\nu)} + \frac{8}{5}\eta\nu\right]\left[1 + \frac{8}{5}\eta\,(3\eta-2)\,\nu g_0(\nu)\right] + \frac{(2+\alpha)\,8\eta\nu^2 g_0(\nu)}{15\pi^{1/2}}$$

$$f_3(\nu) = \frac{25\pi^{1/2}}{16\eta\,(41-33\eta)}\left\{\left[\frac{1}{g_0(\nu)} + \frac{12}{5}\eta\nu\right]\left[1 + \frac{12}{5}\eta^2\,(4\eta-3)\,\nu g_0(\nu)\right] + \frac{64}{25\pi}\,(41-33\eta)\,\eta^2\nu^2 g_0(\nu)\right\}$$

$$f_4(\nu) = \frac{25\pi^{1/2}}{16\eta\,(41-33\eta)}\left[\frac{1}{\nu g_0(\nu)} + \frac{12}{5}\eta\right]\frac{12}{5}\eta\,(2\eta-1)\,(\eta-1)\,\frac{d}{d\nu}[\nu^2 g_0(\nu)]$$

$$f_5(\nu) = \frac{48\eta\,(1-\eta)\,\nu^2 g_0(\nu)}{\pi^{1/2}}$$

$$f_6(\nu) = \frac{\pi\sqrt{3}\nu g_0(\nu)}{4\nu_m f_3(\nu)}$$

$$f_7(\nu) = \frac{\pi\nu g_0(\nu)}{2\sqrt{3}\nu_m f_3(\nu)}$$

$$f_8(\nu) = \frac{\pi\nu g_0(\nu)}{2\sqrt{3}\nu_m f_2(\nu)}$$

$$f_9(\nu) = \frac{8\eta\nu^2 g_0(\nu)}{3\pi^{1/2}}$$

TABLE 2. Dimensionless functions.

Q_t, a bed height H_1 is first estimated, and the values of ν and T^* at different Y positions can be calculated through an iteration process. By integrating the solid fraction obtained along the Y-direction, the mass holdup of granular materials can be obtained:

$$M_t(cal.) = \frac{H}{d_p}\int_0^1 \nu\,\mathrm{d}Y. \tag{18}$$

If this value is not close enough to M_t, a new H_1 will be generated by a variable-step extrapolation method for the next loop of calculation; otherwise the program will output the final solution of H as well as $\nu(Y)$ and $T^*(Y)$ for the base state. The code is written in FORTRAN language and run on the platform of FORTRAN POWER STATION. The spatial resolution (grid size effect) of the numerical method is shown in tables 3 and 4 (in Appendix B) for two characteristic points. The results show reasonable convergence for grid-point number exceeding 50.

Next, the stability of these steady solutions to small perturbations is studied. Here the motion of the material under vibration is no longer considered to be steady, and the variables U^*, V^*, ν, T^* in the governing equations (1)–(3) and boundary conditions (7)–(10) are expressed as the base-state solutions U_0, V_0, ν_0, T_0 (note that U_0 and V_0 are zero) plus small perturbations U', V', ν', T':

$$\begin{bmatrix} U^* \\ V^* \\ \nu \\ T^* \end{bmatrix} = \begin{bmatrix} U_0(Y) \\ V_0(Y) \\ \nu_0(Y) \\ T_0(Y) \end{bmatrix} + \begin{bmatrix} U' \\ V' \\ \nu' \\ T' \end{bmatrix} = \begin{bmatrix} U_0(Y) \\ V_0(Y) \\ \nu_0(Y) \\ T_0(Y) \end{bmatrix} + \begin{bmatrix} U_e(Y) \\ V_e(Y) \\ \nu_e(Y) \\ T_e(Y) \end{bmatrix} \exp(\Omega\tau)\exp(\mathrm{i}K_x X). \tag{19}$$

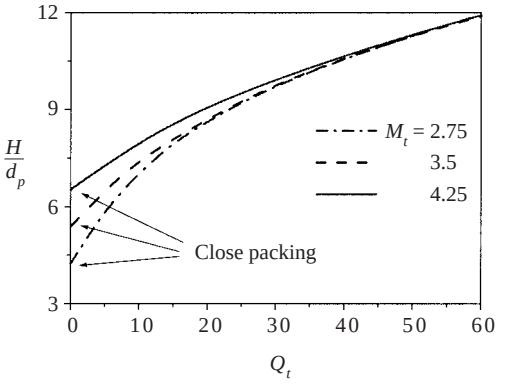

FIGURE 2. Bed height as a function of energy input.

The perturbations here have the typical form adopted by Wang *et al.* (1997) and are periodic in the horizontal dimension. The detailed form of the linearized governing equations and boundary conditions can be found in Appendix A.

By adopting the method used by Wang *et al.* (1997), a set of ordinary differential equations in the variables U_e, V_e, v_e and T_e, subject to two-point boundary conditions, is obtained and constitutes an eigenvalue problem for Ω. This is converted to a matrix eigenvalue problem by taking the finite-difference scheme, and the resulting eigenvalues are computed with Matlab for sequential values of K_x to generate a dispersion relation for each set of operating parameters of the problem. Correspondingly, the eigenvectors can also be obtained for any area of interest. The eigenvalues are then used to determine the stability of the original base state, and the eigenvectors related to those unstable areas give important information about the new patterns that will form. The grid size effect on the calculated eigenvalues is shown in tables 5 and 6 (Appendix B) for two characteristic points. The results show reasonable convergence for the grid-point number exceeding 200.

From the above analysis for both the base state and the perturbation state, it can be seen that the only two operating parameters introduced are M_t and Q_t. However, two different parameters are sometimes used by some researchers: the original bed height, H_0, and the dimensionless acceleration amplitude, Γ (usually defined as $4\pi^2 Af^2/g$, where A is the vibration amplitude and f is the frequency). M_t is directly related to H_0 by equation (18) if the solid fraction at the static state is fixed, while the relationships among energy input, dimensionless acceleration and frequency are rather complex and can only be determined by further theoretical and experimental work. However, based on the theory of vibration, it can be concluded that the energy flux will increase with increasing acceleration and decreasing frequency.

3. Base-state solution

The height of the granular bed at typical operating conditions is shown in figure 2. For a certain mass holdup, the bed height increases with increased energy input. And a higher mass holdup corresponds to a greater bed height when the energy is small; however, if Q_t is large enough (the particles are fully fluidized), the layer heights for different values of mass holdup are almost the same. As stated above, a higher Γ represents a higher Q_t, thus figure 2 also shows that an increase in Γ results in an

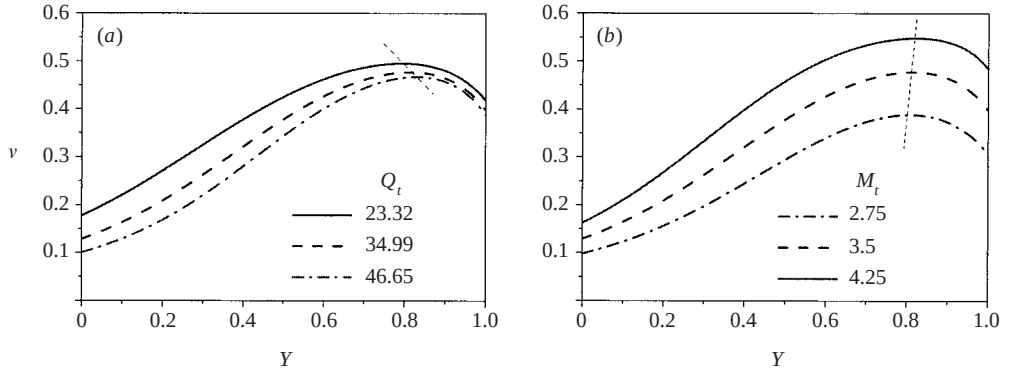

FIGURE 3. (*a*) Solid fraction distribution in the vertical direction for different values of energy input and $M_t = 3.5$. (*b*) Solid fraction distribution in the vertical direction at different values of mass holdup and $Q_t = 34.99$. The thin dashed lines are the solid fraction maxima.

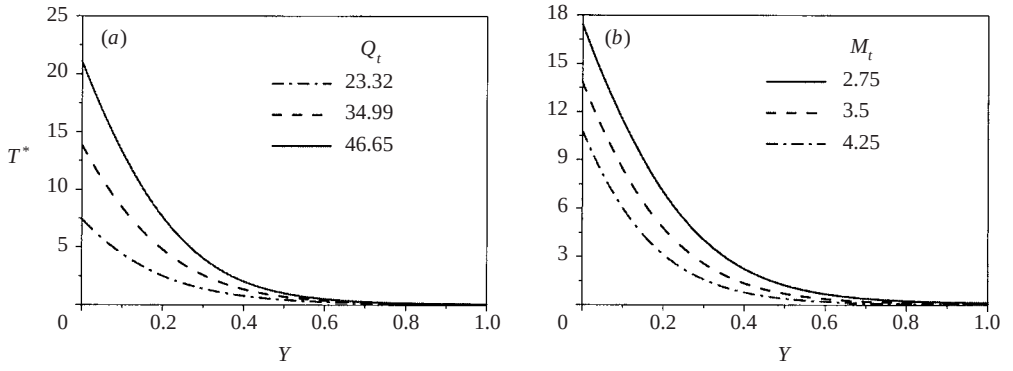

FIGURE 4. (*a*) Granular temperature distribution in the vertical direction at different values of energy input and $M_t = 3.5$. (*b*) Granular temperature in the vertical direction at different values of mass holdup and $Q_t = 34.99$.

increase in bed height. Such a tendency agrees well with that observed in experiments by Hunt, Hsiau & Hong (1994) and Brennen, Ghosh & Wassgren (1996).

The distribution of solid fraction in the Y-direction is shown in figure 3. For a given pair of M_t and Q_t, the solid fraction tends to increase at first up the layer height and then decrease after a certain vertical position, forming a peak of density (marked by a light dashed line) usually at $Y_c = 0.7$–0.9. As shown in figure 3(*a*), more energy input results in a lower solid fraction at a fixed mass holdup, which is followed by the expansion of the layer height; it also results in a shifting of Y_c to a higher value. Figure 3(*b*) indicates that the solid fraction increases with increased mass holdup for the same energy input, accompanied by a slightly increase in Y_c. The occurrence of the densest part in the mid-bed may be due to the joint contributions of the energy input from the bottom that scatters the particles and the unbounded movement of particles at the free surface.

The temperature profile in the Y-direction is shown in figure 4. It can be seen that the particle temperature decreases rapidly from the bottom to the top as a result of the inelastic collisions between particles that dissipates the pseudo-thermal energy originating from the bottom plate. When the energy supplied to a certain

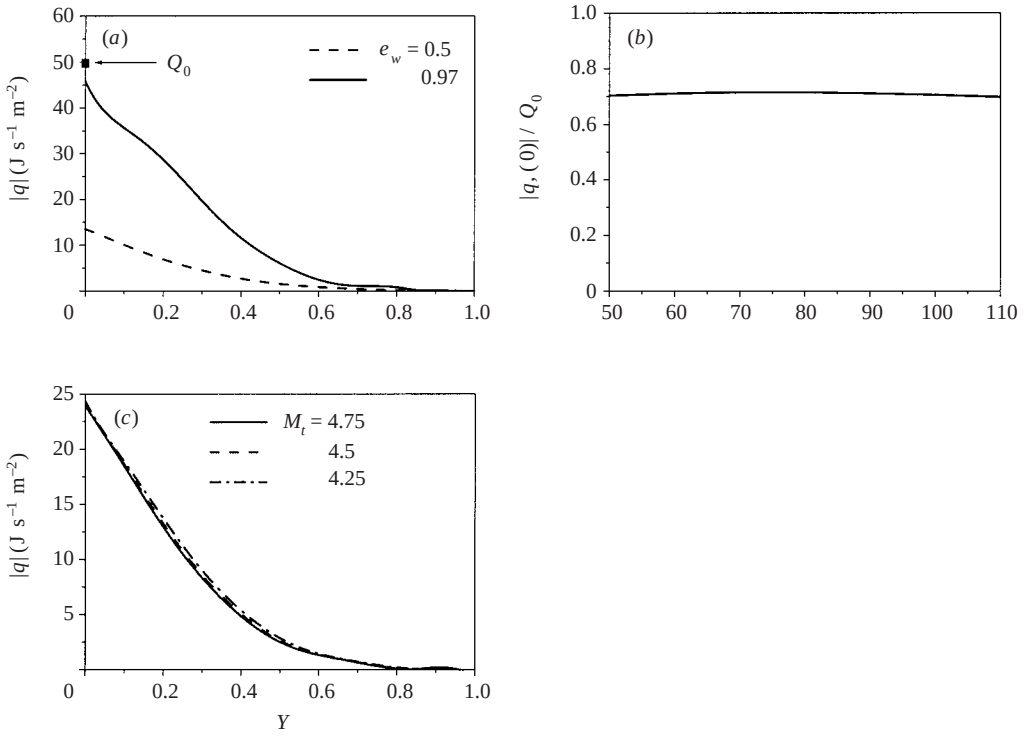

FIGURE 5. Energy distribution in the vertical direction. (*a*) Pseudo-thermal energy flux at $e_w = 0.5$ and 0.97 (M_t, Q_t) = (4.25, 58.31). (*b*) Energy fraction transferred upwards at different values of energy input ($e_w = 0.5$ and $M_t = 4.75$). (*c*) Energy flux at different values of mass holdup ($e_w = 0.5$ and $Q_t = 104.96$).

mass increases, the random motion of particles becomes more violent, resulting in the increasing particle temperature in figure 4(*a*). The particle temperature reduces if the vibration energy is used to activate more mass, as shown in figure 4(*b*).

It is important to have a detailed analysis of the energy flux in the vertical direction. According to equation (8), part of the energy input from the bottom is dissipated through the particle–wall collisions and the rest is transferred to the particles in upper layers. This is seen in figure 5(*a*), in which a sudden drop in energy occurs at $Y = 0$. This effect can be reduced by increasing e_w, and the energy transferred upwards decreases gradually up the bed height as a result of particle–particle collisions until finally vanishes at the top surface. Figure 5(*b*) indicates that the fraction of energy transferred to upper layers is almost the same at different values of Q_t. In contrast, figure 5(*c*) implies that the energy distribution in the vertical direction varies little for different mass holdups. All this means that the division of energy between dissipation and transfer is mainly dependent on the inelastic collision properties (e_p and e_w) rather than the operating conditions (M_t and Q_t).

The wall properties must influence the base-state solution. As shown in figure 6, when $M_t = 3.5$, the distribution of solid fraction and particle temperature for $Q_t = 23.32$ at $e_w = 0.97$ is the same as that for $Q_t = 69.97$ at $e_w = 0.5$. Both refer to energy source walls although the increase in the particle–plate restitution coefficient can reduce the energy needed to reach the same base-state profile.

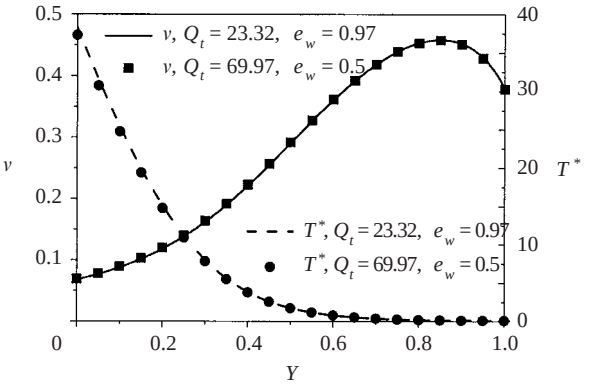

FIGURE 6. Profiles of solid fraction and granular temperature in the case of a source wall and a sink wall.

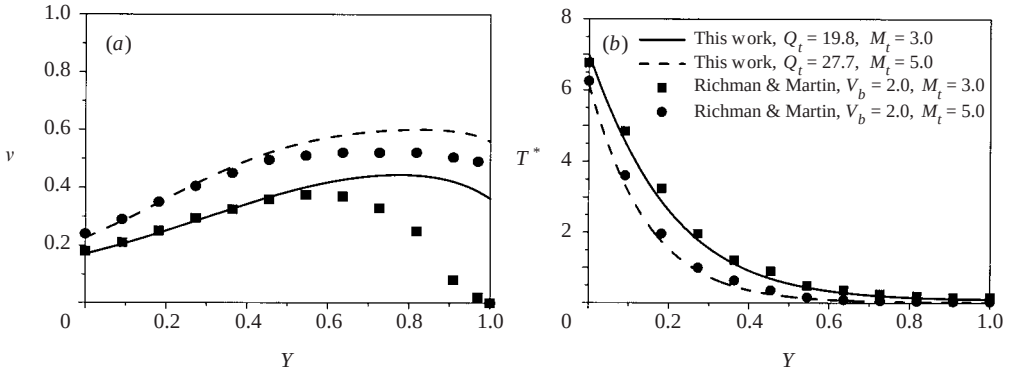

FIGURE 7. Comparison of the results of this work and predictions of Richman & Martin (1992): (*a*) solid fraction, (*b*) granular temperature.

Richman & Martin (1992) calculated the profiles of solid fraction and particle temperature in a vibrating bed based on the grain kinetic theory. The results were confirmed by Lan & Rosato (1995) using a discrete element simulation method. Experimental evidence can be found in Wildman, Huntley & Parker (2001*a*, *b*) and Yang *et al.* (2002). These results are compared with the present work in figure 7. Since no direct relationship exists between the energy input Q_t (our parameter) and the dimensionless root-mean-square velocity V_b (Richman's parameter), the mass holdup (M_t) and the solid fraction at the bottom plate (ν_0) are set equal in order to carry out the comparison. The distribution of granular temperature agrees well; however some differences are observed in the solid fraction profiles, especially at the free surface. When $(M_t, Q_t) = (5.0, 27.7)$, both models predict a 'step change' in solid fraction at the free surface, which remains in our model at $(M_t, Q_t) = (3.0, 19.8)$ while in Richman's model it varies smoothly to zero. The deviation may be due to the different boundary conditions adopted in these two models: Richman & Martin assumed that the normal stress at the top surface is zero instead of the force balance used in the present study.

However, we do not want to make a judgment about the suitability of the two models. In fact, the base-state solution does not always exist in real experiments. If the base state is stable, it can be observed; otherwise, the perturbations in the

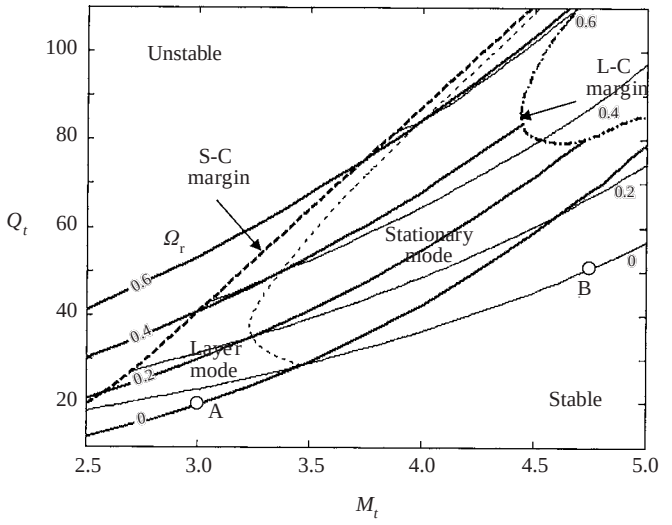

FIGURE 8. Stability diagram showing the contours of Ω_r. $\Omega_r = 0$ is the neutral stability contour, $\Omega_r > 0$ and $\Omega_r < 0$ are the unstable and stable regimes, respectively. The thick and thin solid grey curves are the real parts of the L-C and S-C eigenvalues, respectively. The thin dashed curve is the dividing line between the layer mode and the stationary mode.

experimental conditions will change the original unstable base state into a new stable one. For example, according to the stability diagram in the (M_t, Q_t) plane (figure 8 in §4), the base state at point $(M_t, Q_t) = (5.0, 27.7)$ is stable but that at point $(M_t, Q_t) = (5.0, 80.0)$ is unstable and will evolve into a new state in which the solid fraction smoothly approaches zero at the free surface as Richman's model suggests. (The details will be discussed later in the nonlinear analysis.) In this sense, Richman's model may present the final solution, while the solution obtained here is an intermediate unstable base state. The stability of such base states is discussed in the next section.

4. Stability diagram

Since both the mass holdup and energy input vary from zero to infinity, it is necessary to narrow down the range of operating conditions to be examined. When M_t is small, the granular-material bed will be very shallow. For example, $M_t = 2$ means that the bed height in the static state is only three times the particle diameter, and so it is difficult to form stable patterns. On the other hand, the layer at a large M_t may be so thick that friction plays an important role in the particle–particle interaction, and this is in conflict with the model assumption that friction is not taken into account. If the energy supplied is too small, the base state will be stable because it does not have the energy necessary to form a new state, and the upper limit for the energy input is always determined by the vibration generator used in the experiments. Therefore, the area of interest should reside in the middle of the (M_t, Q_t) plane.

The stability diagram of such an area is shown in figure 8. Because M_t and Q_t are the only two operating parameters used in the simulation, any point in the plane represents a base state whose stability can be determined from this diagram.

Now we consider a point (M_t, Q_t). If N grid points are taken for in vertical direction in the finite difference method, then for a fixed K_x, $(4N\text{-}7)$ eigenvalues will be found,

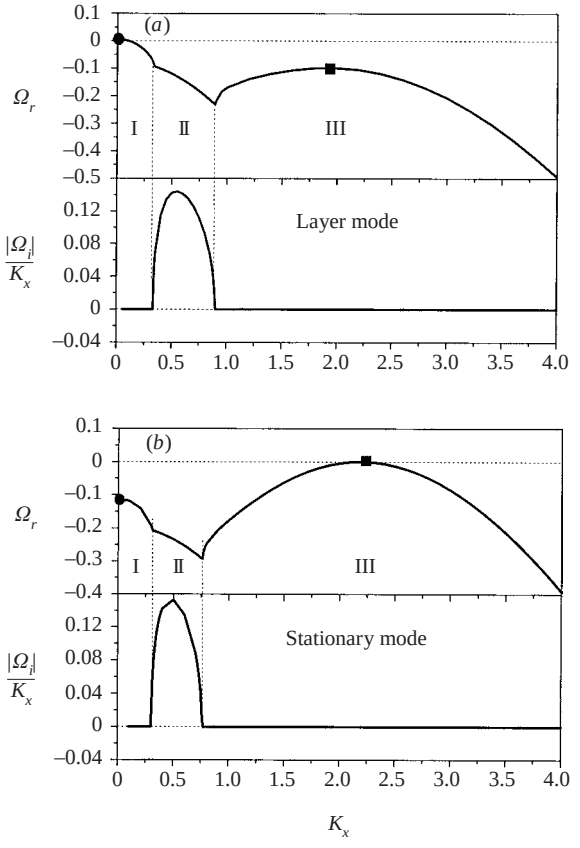

FIGURE 9. (*a*) Dispersion relation at point A (M_t, Q_t) = (3.0, 19.83). (*b*) Dispersion relation at point B (M_t, Q_t) = (4.75, 51.31).

among which we choose the one with the largest real part eigenvalue as the *leading eigenvalue*. The $4N$-7 eigenvalues are obtained by considering the total number of variables: 3(N-2) for the momentum equations (A 2) and (A 3) in the X- and Y-directions and pseudo-thermal equation (A 4), and $N-1$ for the continuity equation (A 1). A group of leading eigenvalues can be obtained by scanning K_x in a wide range, for example, the $\Omega_r - K_x$ curve in figure 9 represents the real part of a set of leading eigenvalues (Ω_r) at different values of K_x. Such a curve may have some local maxima, such as the points marked by the circle and square. The eigenvalues related to these local maxima are called the *chief eigenvalues*, among which the one with the largest real part is referred to as the *dominant eigenvalue* (denoted by the circle shown in regime I for figure 9(*a*) and the square shown in regime III for figure 9(*b*)). If Ω_r corresponding to the dominant eigenvalue is positive, perturbations in the form of equation (19) will increase exponentially with time. We refer to the corresponding base state as 'unstable'; otherwise, the perturbations will vanish and hence the base state is 'stable'. Here, Ω_r is an index for the growth rate of perturbations, and $|\Omega_i|/K_x$ is the phase velocity of the dominant density wave pattern.

The solid curves in figure 8 are contours of the real part of the chief eigenvalues, marked with the relevant Ω_r values. There are two sets of contours: one is called set L (shown as thicker curves), corresponding to the point marked by a circle in figure 9

where K_x is zero; the other is called set S (shown as thinner curves), corresponding to the point marked by the square where K_x is positive. These two sets mix together and the contours from one set cross those from the other. Moreover, all the contours show that the growth rate increases with increased energy and reduced mass holdup. Thus, the contours with a zero value of Ω_r form the dividing line between the stable and unstable areas: stable base states are found in the bottom-right corner of the stability diagram, and in the top-left corner are the unstable base states.

The thin dashed curve in figure 8 consists of the intersections of two contours that have the same value of Ω_r but come from two different sets. Thus, any point on this curve has two equal chief eigenvalues, one in set L and the other in set S. For any point to the left of the curve, the contour from set L has a larger Ω_r than that from set S, which indicates that the chief eigenvalue from set L (denoted the L-C eigenvalue) is the dominant eigenvalue; for points to the right of the curve, the chief eigenvalue from set S (the S-C eigenvalue) is the dominant eigenvalue.

As stated above, the L-C eigenvalue always appears at the point where K_x is zero. The perturbation form in equation (19) implies that the new pattern will be uniform in the X-direction and only vary in the Y-direction. This indicates a layer mode. As shown in figure 9, the phase velocity related to the S-C eigenvalue is always zero, which means that the waves are standing waves and constitute the stationary mode. Therefore, the light dashed curve is also the division between these two modes: to the left the dominant mode is the layer mode, and to the right it is the stationary mode.

However, neither set L and set S is distributed throughout the whole region. The heavy dashed curve in figure 9 shows the beginning of set S – contours in set S never appear in the area to the top-left of the heavy dashed curve. On the other hand, the heavy dashed-dotted curve in the top-right of figure 9 encloses a zone where only set S exists.

To obtain more insight, we now fix the mass holdup and examine the change of Ω_r with increasing energy input. The results are shown in figure 10(a–c), with the dimensionless mass holdup $M_t = 2.75$, 3.35 and 4.75, respectively.

As shown in figure 10(a), if the energy input is low (curve a'), the growth rate is always negative, indicating that the corresponding state is stable for all kinds of perturbation. When Q_t is increased to a certain critical value, the real part of the L-C eigenvalue reaches zero (b'), and the base state is at the least-stable point. This corresponds to the point on the thick grey contour with the value of zero in figure 8. With more energy input, the base state becomes unstable, and the L-C eigenvalue is always dominant (c' and d'). On the other hand, the S-C eigenvalue tends to appear at a smaller K_x for a higher energy input, and finally disappears and 'blends in' with the L-C eigenvalue (e').

Similarly, the base state in figure 10(b) becomes unstable when Q_t is increased to 26.24 because the real part of the L-C eigenvalue is zero (a'). But when $Q_t = 30.32$, the L-C eigenvalue is equal to the S-C eigenvalue (b'), corresponding to a point on the lower branch of the light dashed curve in figure 8. Beyond that point, the S-C eigenvalue will be dominant (c') until two the chief eigenvalues are again equal on the upper branch of the light dashed curve (d'). As Q_t increases, the L-C eigenvalue dominates again (e') and finally the S-C eigenvalues disappear (f').

The situation at $M_t = 4.75$ is different from the previous case, as shown in figure 10(c). The real part of the S-C eigenvalue first reaches zero at $Q_t = 51.31$ (a'), indicating that the stationary mode is dominant here. For curve (b'), the real part of the L-C eigenvalue also reaches zero, but the S-C eigenvalue remains dominant. When the energy input Q_t continues to increase, the L-C eigenvalue begins to vanish

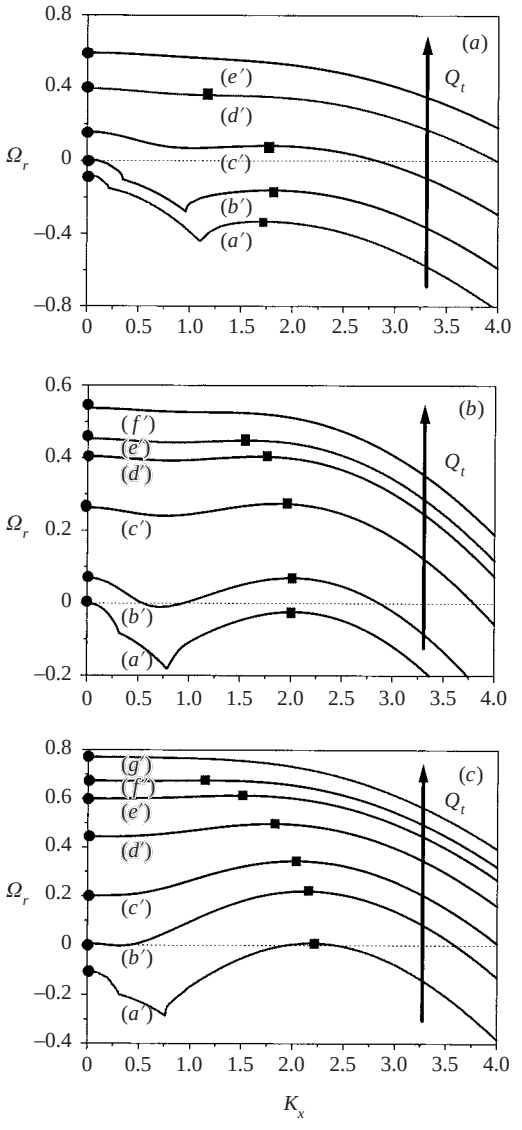

FIGURE 10. The growth rate at different wavenumbers: (*a*) $M_t = 2.75$ and (*a′*) $Q_t = 11.66$, (*b′*) $Q_t = 15.74$, (*c′*) $Q_t = 29.15$, (*d′*) $Q_t = 34.99$, (*e′*) $Q_t = 46.65$. (*b*) $M_t = 3.35$ and (*a′*) $Q_t = 26.24$, (*b′*) $Q_t = 30.32$, (*c′*) $Q_t = 40.82$, (*d′*) $Q_t = 49.56$, (*e′*) $Q_t = 52.48$, (*f′*) $Q_t = 58.31$. (*c*) $M_t = 4.75$ and (*a′*) $Q_t = 51.31$, (*b′*) $Q_t = 68.80$, (*c′*) $Q_t = 79.30$, (*d′*) $Q_t = 99.13$, (*e′*) $Q_t = 114.29$, (*f′*) $Q_t = 126.45$, (*g′*) $Q_t = 134.11$.

(*c′*). In this case, there is only one peak in the Ω_r–K_x curve (*d′*). When $Q_t = 114.29$ the L-C eigenvalue reappears (*e′*); it then catches up with the S-C eigenvalue and the stationary mode becomes a layer mode at $Q_t = 126.45$ (*f′*). Finally it becomes the only existing chief eigenvalue (*g′*).

It is also of interest for engineering purposes to examine the stability profile by varying the mass holdup at a fixed energy input Q_t. As shown in figure 11, the system remains a layer mode when the mass holdup is small (*a′*), and the L-C eigenvalue is the only chief eigenvalue until M_t reaches 3.1 (*b′*). The newborn S-C eigenvalue

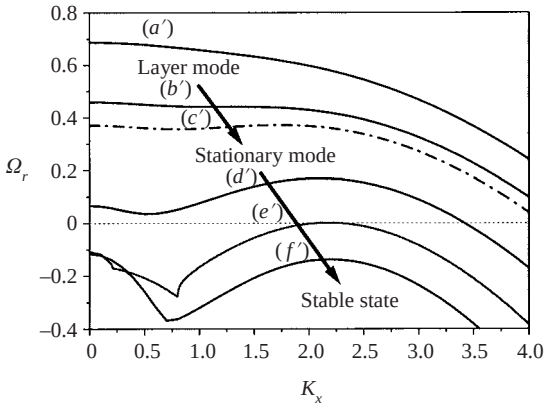

FIGURE 11. The mode evolution occurring at $Q_t = 46.67$ by increasing the mass holdup. (a') $M_t = 2.5$, (b') $M_t = 3.1$, (c') $M_t = 3.32$, (d') $M_t = 4.0$, (e') $M_t = 4.56$, (f') $M_t = 5.0$.

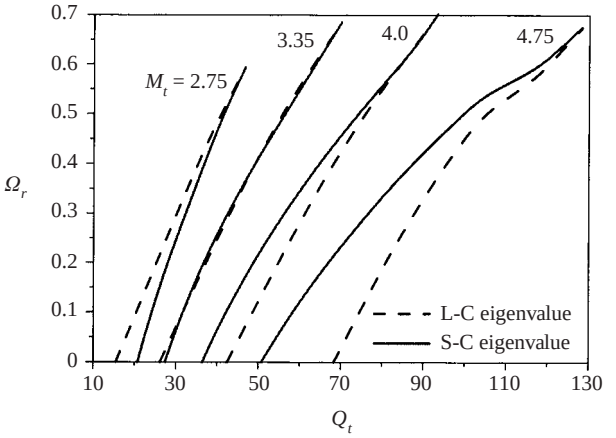

FIGURE 12. The growth rate of the L-C and S-C eigenvalues as a function of M_t and Q_t.

continues to grow until it becomes the dominant eigenvalue after $M_t = 3.32$ (c'), and correspondingly the system enters the stationary mode. Such a situation continues (d') until the real part of the dominant eigenvalue decreases to zero (e'), after which the base state is always stable (curve f').

Figure 12 summarizes the dependence of the real part of the chief eigenvalues on the energy input and mass holdup. For a fixed M_t, the chief eigenvalues form two Ω_r–Q_t curves (one is for L-C eigenvalues and the other for S-C eigenvalues), and the dominant eigenvalue for the base state depends on which curve is at the top. When the mass holdup increases, the slope of the Ω_r (S-C)–Q_t curve tends to decrease significantly while that of Ω_r (L-C)–Q_t decreases little. Therefore, although the Ω_r (L-C)–Q_t curve is above the Ω_r (S-C)–Q_t curve at a small mass holdup (i.e. $M_t = 2.75$), the opposite situation occurs at high M_t values (i.e. $M_t = 4.25$ and 4.75). The transition takes place at $M_t = 3.35$ where the two competing mechanisms – formation of a layer mode or a stationary mode – are of about the same magnitude.

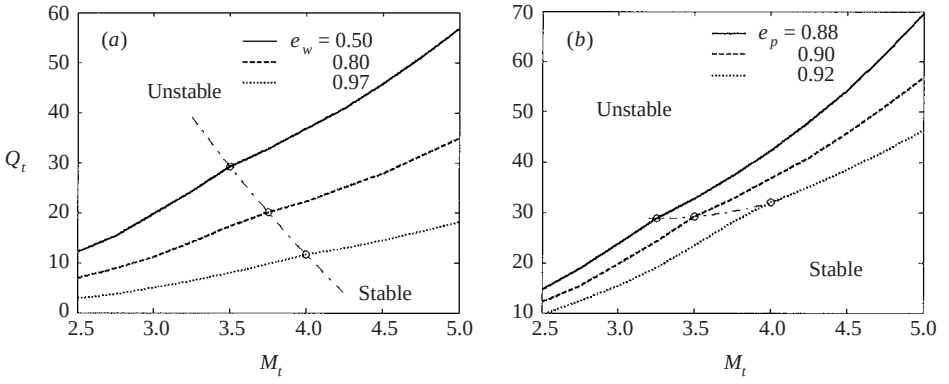

FIGURE 13. The effect of (*a*) e_w and (*b*) e_p on the stability diagram.

The effects of e_w and e_p on the stability diagram are examined in figure 13. The solid, dashed and dotted curves are the neutral stability contours ($\Omega_r = 0$) and correspond to the least-stable states. The thin dashed-dotted curve joins the points (denoted by circles) that separate the layer mode and the stationary mode. As shown in figure 13(*a*), the energy needed to attain the least-stable state increases with deceasing e_w, and the range of the stationary mode is enlarged. If the case requiring a higher energy input at the least-stable state is regarded as 'more stable', this means that a high value of e_w will destabilize the system. Figure 13(*b*) indicates that e_p has the same effect on destabilization as e_w.

Therefore, it can be concluded that an increase in Q_t, e_p or e_w will cause the base state to be more unstable and these variables are referred to as 'destabilizing' factors. On the other hand, any change that results in an increase of M_t (such as increasing m_p) can suppress the occurrence of instability, thus M_t is viewed as a 'stabilizing' factor. Significant differences exist between destabilizing and stabilizing factors: the former is concerned with energy input while the latter is related to the mass loading of the system; the former takes the system away from the base state while the latter keeps it unchanged. The balance between these two opposing factors determines whether a base state is stable or not.

However, this does not mean that e_p and e_w reach a value of 1 (that is, collisions are fully elastic). In that case, all the vibration energy will be changed into mechanical energy, and no stable base state can be obtained because the velocity of the particles will increase infinitely. And, although Shinbrot (1997) stated that the surface patterns can also form in the absence of gravity according to simulation results, this is not practical because an endless expansion of the bed height will occur in this case.

For a mass holdup higher than a critical value M_{tc}, the stationary mode begins to dominate in the M_t–Q_t plane. The case reported in figure 10(*c*) is such an example where standing waves appear when Q_t is increased beyond $Q_{tc1} = 51.31$ but disappear again above $Q_{tc2} = 126.45$. A detailed investigation of the wavelengths λ_x between Q_{tc1} and Q_{tc2} is shown in figure 14. The wavelength increases slowly on increasing the energy above Q_{tc1}; however, a sharp increase in λ_x occurs when the energy approaches Q_{tc2} until the wavelength is so large that no waves can be observed in a dimension-limited container, denoting the transition from the stationary mode to the layer mode. For a shallow bed with mass holdup lower than M_{tc}, our model suggests that the flat layer is the dominant pattern without the occurrence of standing waves.

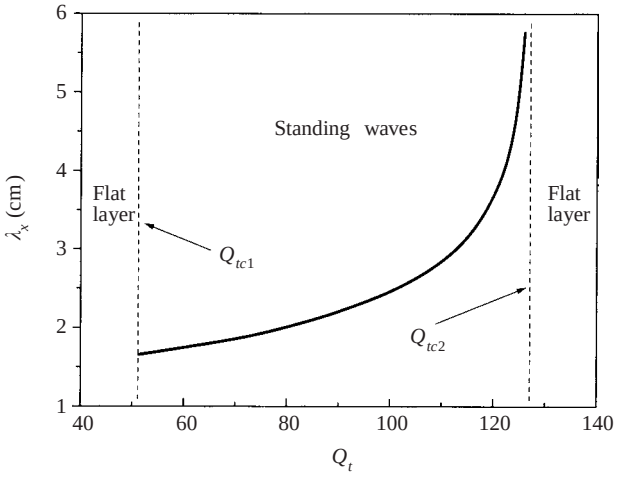

FIGURE 14. The variation of wavelength with Q_t for $M_t = 4.75$.

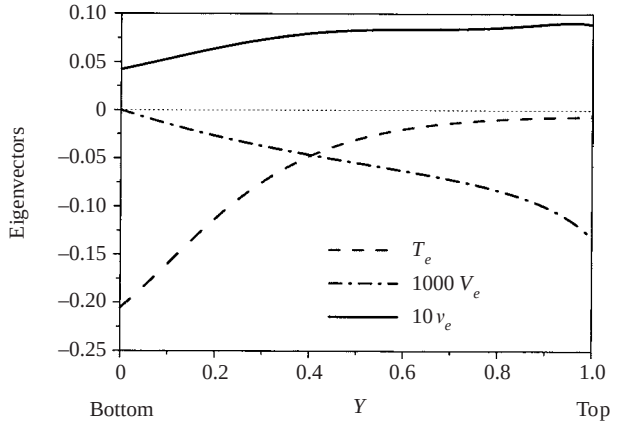

FIGURE 15. Distribution of eigenvectors (V_e, v_e, T_e) in the Y-direction. (M_t, Q_t) = (3.0, 19.83), $K_x = 0$.

5. Patterns in the vertical direction

In addition to the stability diagram, it is also important to find the new patterns that form as a result of the destruction of the original unstable base state. Two points (denoted by A and B in figure 8) in different modes are chosen to illustrate this problem.

The dispersion relations of point A ($M_t = 3.0$, $Q_t = 19.83$) are shown in figure 9(*a*). The dominant eigenvalue is at $K_x = 0$, indicating a layer mode here. Regimes I and III have a phase velocity of zero and thus imply a standing wave in the X-direction, while regime II corresponds to a travelling wave.

It can be seen from figure 15 that the values of eigenvectors at $K_x = 0$ are not of the same order of magnitude. The particle temperature is larger than the solid fraction, and the Y-component velocity is the smallest. The eigenvector for the velocity in the X-direction is not shown here because its real part is always zero. The absolute value of the particle temperature decreases from the bottom to the top but that of the solid

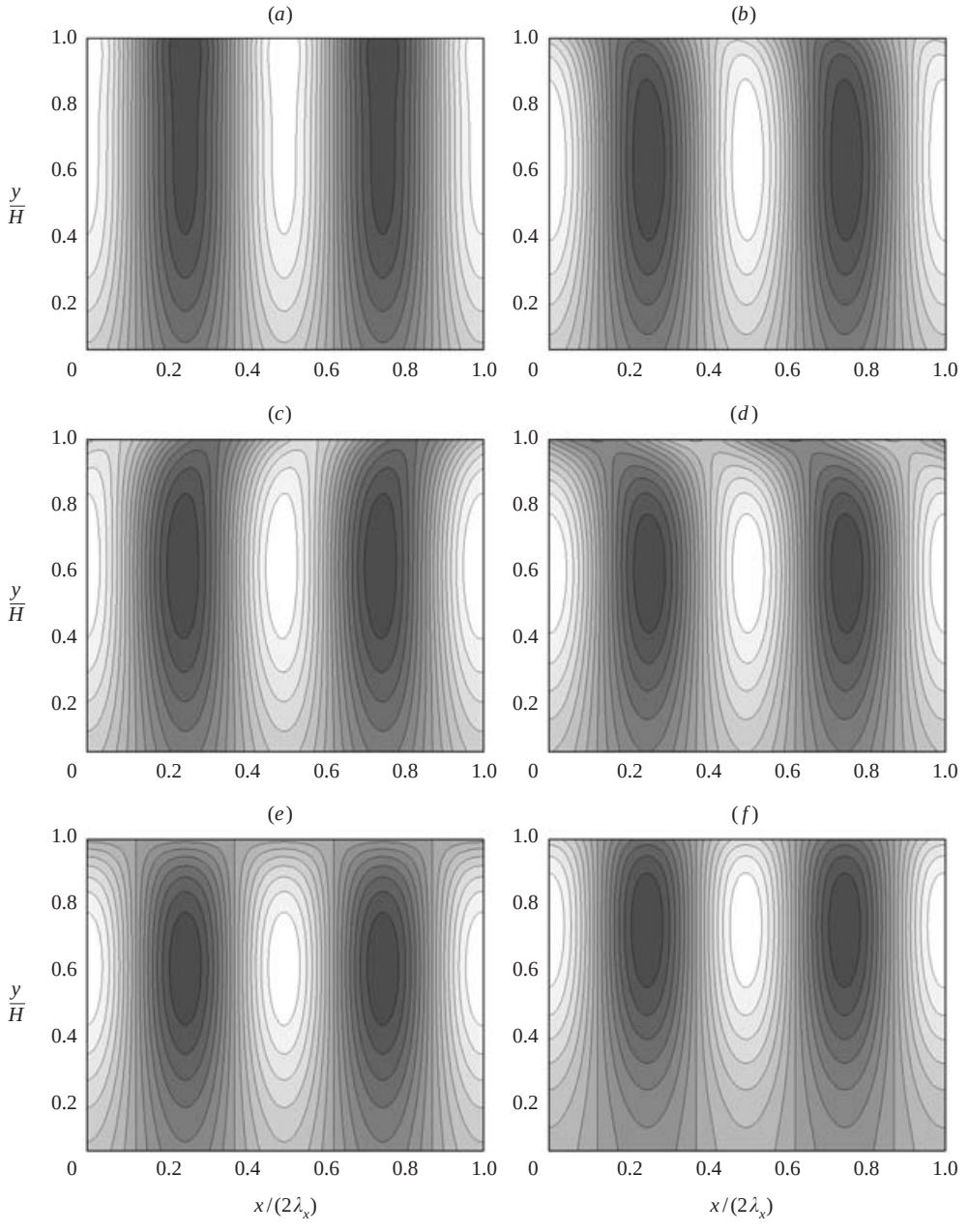

FIGURE 16. Patterns for different K_x at $(M_t,\ Q_t) = (3.0, 19.83)$: (*a*) $K_x = 0.1$, (*b*) $K_x = 0.4$, (*c*) $K_x = 0.55$, (*d*) $K_x = 0.8$, (*e*) $K_x = 2.0$, (*f*) $K_x = 4.0$.

fraction tends to increase with height. The Y-component velocity is zero at the bottom plate due to the boundary condition (given in (A 6)), and achieves its maximum at the free surface.

The patterns of solid fraction forming in the vertical direction for $K_x \neq 0$ are shown in figure 16. The darker region in the figures represents the denser parts in the (X, Y) plane. Panel (*a*) shows the standing wave in regime I; its high density fluctuations

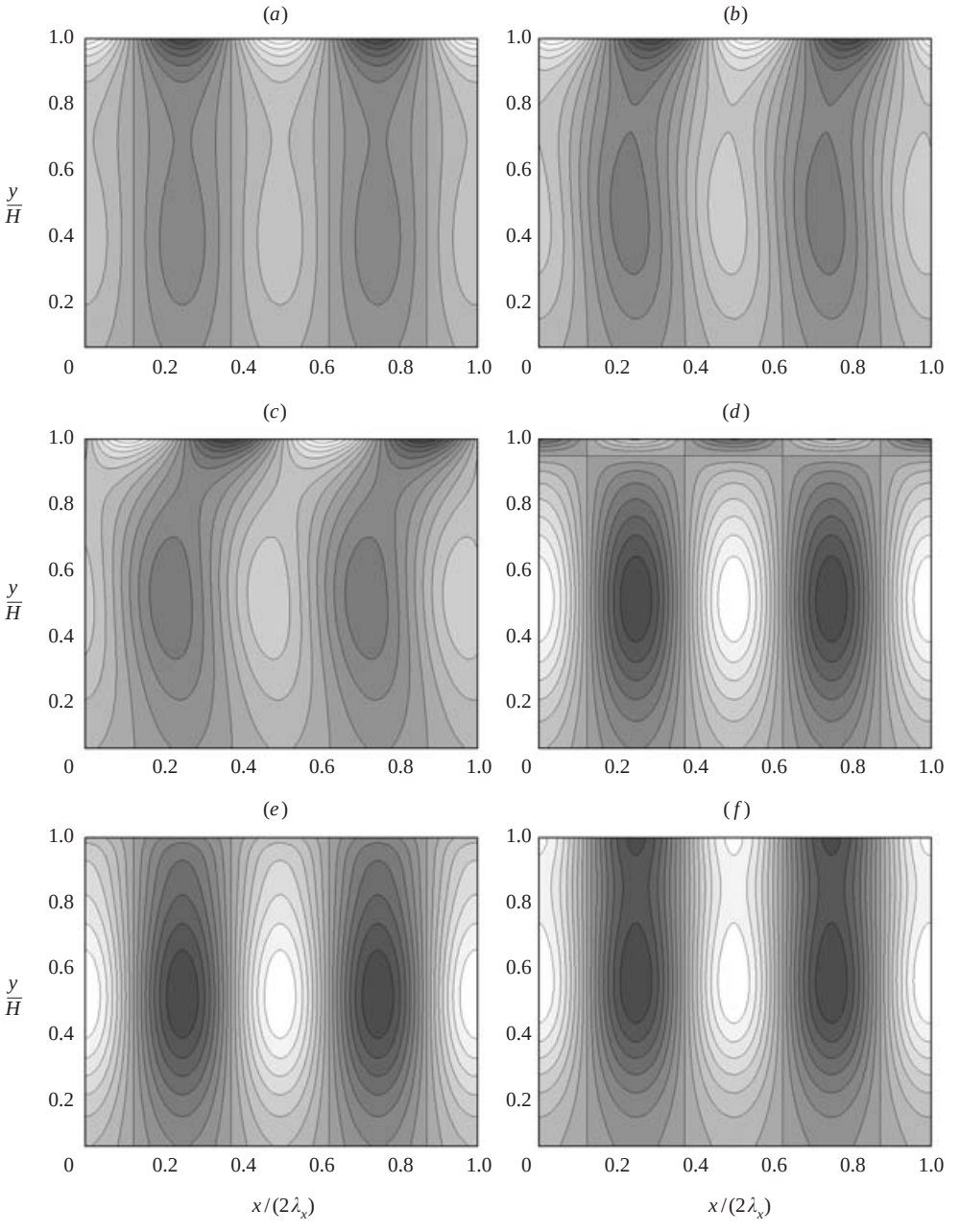

FIGURE 17. Patterns for different K_x at $(M_t, Q_t) = (4.75, 51.31)$: (*a*) $K_x = 0.1$, (*b*) $K_x = 0.5$, (*c*) $K_x = 0.7$, (*d*) $K_x = 0.8$, (*e*) $K_x = 2.2$, (*f*) $K_x = 4.0$.

are observed on the surface of the layer. Panels (*b*), (*c*) and (*d*) are in the travelling wave regime where the wave speed is determined by $|\Omega_i|/K_x$. Unlike the standing waves in panel (*a*), the patterns here are not symmetric about the line $x/2\lambda_x = 0.5$. By comparing panels (*b*) and (*c*), it can also be seen that the speed and direction of the travelling waves may influence the pattern appearance. The patterns in regime III, denoted by panels (*e*) and (*f*), are different from those in regime I. The dark (light)

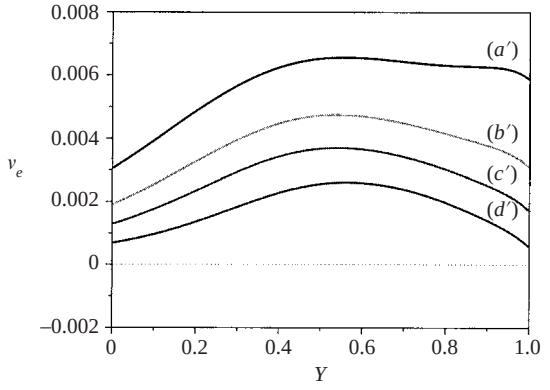

FIGURE 18. Eigenvector of solid fraction corresponding to $K_x = 0$ for different energy inputs at $M_t = 3.0$: (a') $Q_t = 23.32$, (b') $Q_t = 29.15$, (c') $Q_t = 34.99$, (d') $Q_t = 46.65$.

parts have the shape of islands with the highest (lowest) solid concentration in the centre. For a large value of K_x, the centres of islands tend to move closer to the free surface.

The dispersion relations of point B ($M_t = 4.75$, $Q_t = 51.31$) are shown in figure 9(b). This point is located in the least-stable stationary mode with its dominant eigenvalue occurring at $K_x = 2.2$. Similar to point A, the patterns in regimes I and III are standing waves while those in regime II are travelling waves.

Figure 17 shows the patterns at different values of K_x. Panel (a) has two cores in the Y-direction: one is in the lower half and the other is near the surface. These two cores/voids have similar solid fractions, that is both are dense or both are dilute. In the travelling wave of panel (b), the upper core begins to move away from its original horizontal position to above the neighbouring lower centre, as shown in panel (c). In panel (d), where the standing wave in regime III begins, this movement has been completed, and the pattern now has a dense core and a dilute void in the vertical direction. Panel (e) has only one core left in the Y-direction and the islands mentioned above appear. For higher values of K_x, the single central cluster will break into two cores again, as shown in panel (f).

The most important density wave patterns are the dominant patterns. Figure 18 shows the dominant eigenvector of the solid fraction at different energy inputs when $M_t = 3.0$ (in the dominant layer mode regime). If the energy is low (curve a'), the solid fraction increases up the bed height until it reaches a critical value, and changes little beyond that. With increasing vibration energy, the solid fraction tends to form a peak in the middle of the bed (b', c', d').

Figure 19 shows the dominant pattern of solid fraction at different energy inputs with a mass holdup $M_t = 4.75$ (in the dominant stationary mode regime). As shown in panels (a) to (f), the increase of input energy will change the patterns gradually from one core in the middle to three cores in the vertical direction: two dense (dilute) cores in the lower part and one dilute (dense) core at the surface.

6. Surface patterns

In order to trace the surface patterns, a three-dimensional form of perturbation is introduced as follows instead of equation (19):

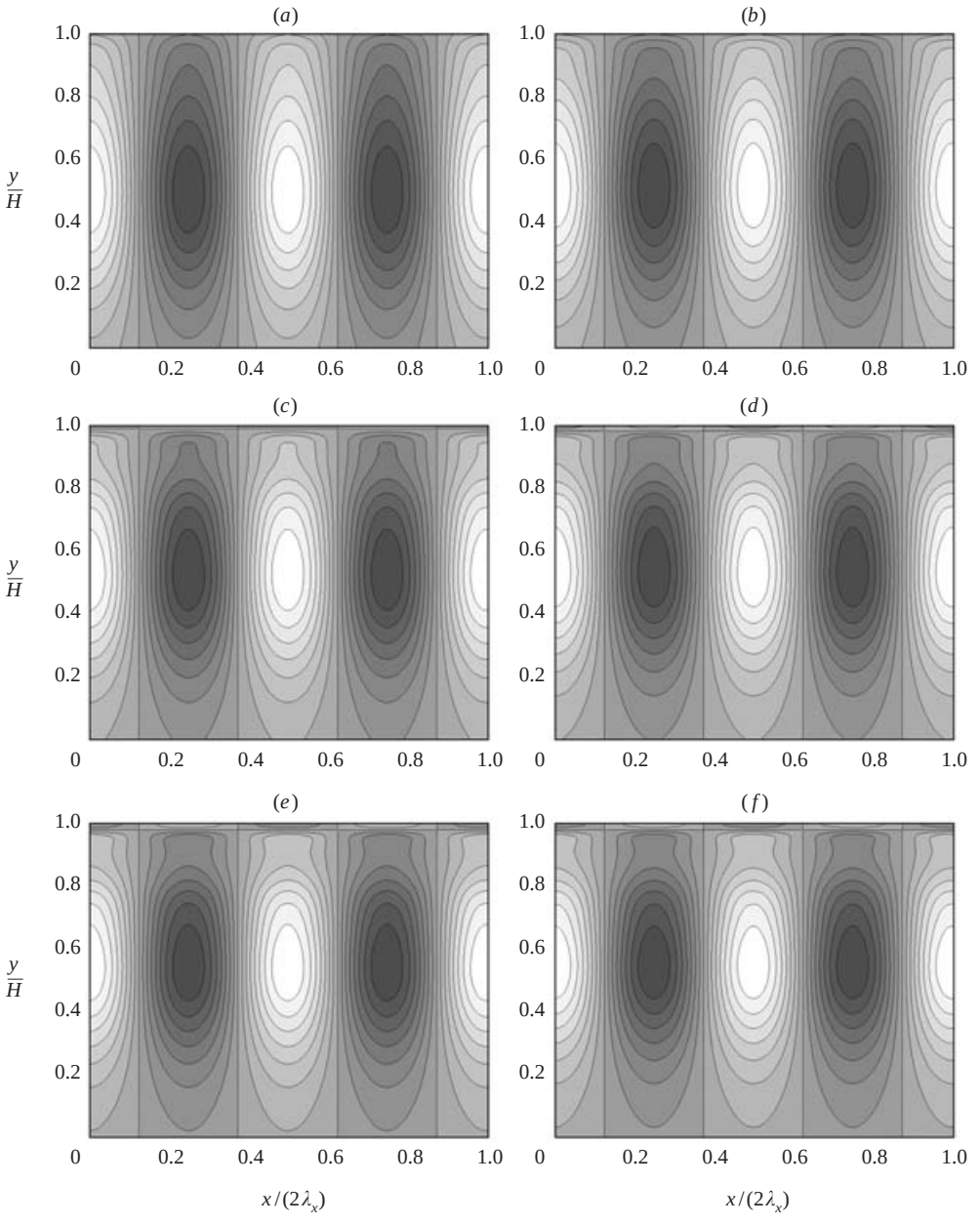

FIGURE 19. Patterns corresponding to the dominant eigenvalue for different energy inputs at $M_t = 4.75$: (*a*) $Q_t = 58.31$, (*b*) $Q_t = 68.80$, (*c*) $Q_t = 87.46$, (*d*) $Q_t = 99.13$, (*e*) $Q_t = 110.79$, (*f*) $Q_t = 122.45$.

$$[U', V', W', \nu', T'] = [U_e(Y), V_e(Y), W_e(Y), \nu_e(Y), T_e(Y)] \exp(\Omega\tau) \exp(\mathrm{i}K_x X) \exp(\mathrm{i}K_z Z). \tag{20}$$

Following similar deduction procedures as above, a matrix eigenvalue problem for U_e, V_e, W_e, ν_e and T_e is obtained and then computed with Matlab. Based on the

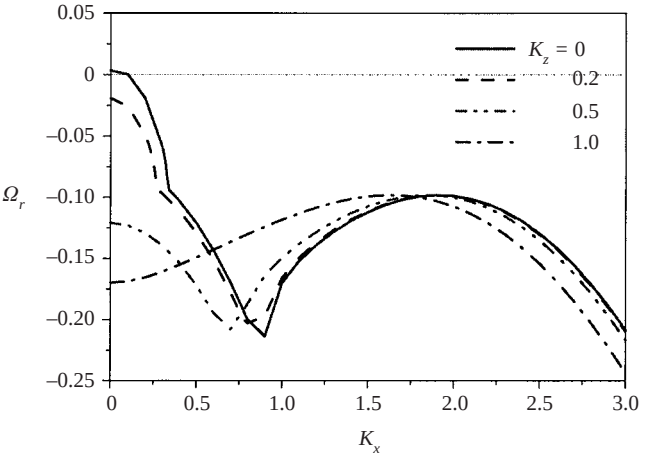

FIGURE 20. Effect of K_z on the Ω_r–K_x curve, $(M_t, Q_t) = (3.0, 19.83)$.

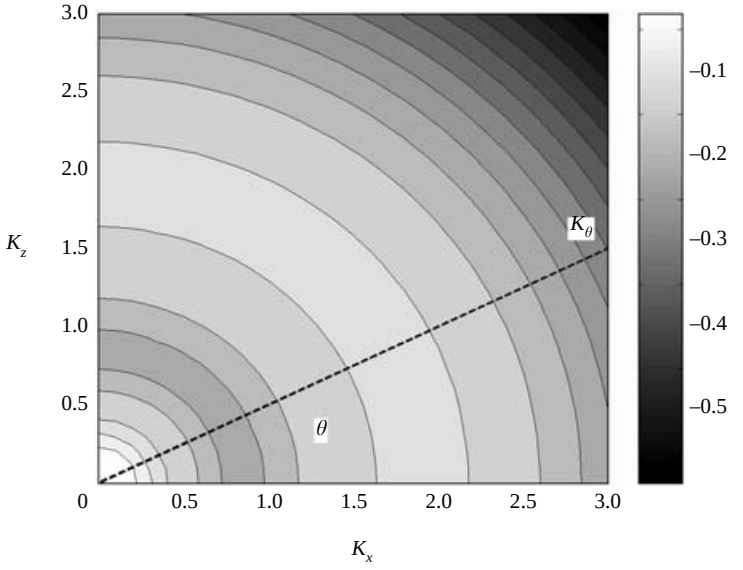

FIGURE 21. Contours of Ω_r in the (K_x, K_z)-plane, $(M_t, Q_t) = (3.0, 19.83)$.

eigenvalues and eigenvectors obtained, the stability of the system under the action of three-dimensional perturbations can be determined.

Although K_z has been introduced, we can still plot the curves of Ω_r vs. K_x as shown in figure 20. While the value of K_z appears to affect the shape of the curves, it cannot be concluded that K_z influences the stability diagram because the stability of the base state for the three-dimensional perturbation cannot be obtained only by examining the Ω_r–K_x curve. The joint contributions of K_x and K_z to Ω_r are shown in figure 21, where the contours of Ω_r appear to be symmetric around the origin in the K_x–K_z plane; that is, the same curve of Ω_r–K_θ will be obtained in any direction for the angle θ in the range $(0 \leqslant \theta \leqslant \pi/2)$. For example, the curve Ω_r–K_x $(\theta = 0)$ has the same shape as Ω_r–K_Z $(\theta = \pi/2)$, indicating that they share the same leading

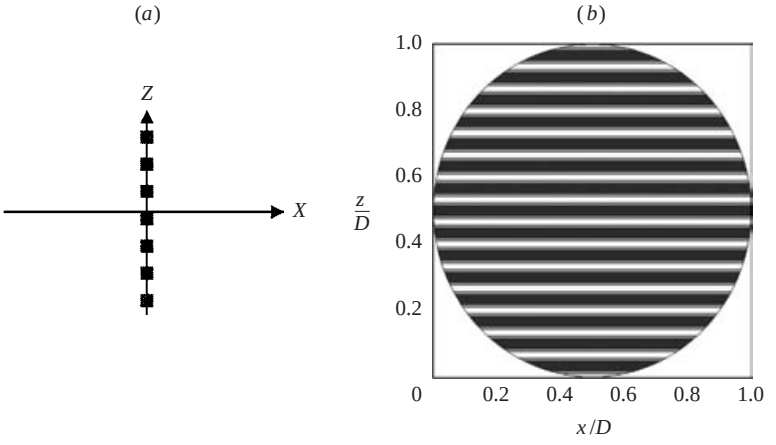

FIGURE 22. Pattern of stripes: (*a*) a perturbation in the *Z*-direction; (*b*) stripes from the simulation, $(M_t,\ Q_t) = (4.75, 51.31)$, $K_x = 2.2$.

eigenvalues. The introduction of K_z does not change the nature of the stability diagram.

This conclusion agrees with the physical reality. Because both the *X*- and *Z*-directions are considered infinite, the space is symmetric about any point in (X, Z)-plane and all directions are indistinguishable. A perturbation in any direction will have the same effect on the base state.

Now we focus on the patterns emerging at the free surface, including stripes, squares, and hexagons. It should be pointed out that the patterns obtained here are the time-average values over one period, which are different from those obtained from experiments (Umbanhowar 1997). Point B (in the stationary mode regime) is selected again for illustration.

As stated above, if a perturbation in the *Z*-direction (as shown in figure 22*a*) acts on the base state given by point B, the patterns shown in figure 17 will develop in the (X, Y)-plane with alternate clusters and voids at the top surface. Figure 22(*b*) shows the top view of the dominant patterns simulated in a round-base container, where the dark and bright parts are the dense and dilute zones, respectively. In fact, as we will explain later, these are not only non-uniformities in solid concentration but also stripes observed in the vertical direction.

According to the principle of superposition of waves, the net displacement of granular material at any point in space or time is simply the sum of the individual wave displacements. Therefore, if two or more perturbations act on the base state, the surface pattern is the combination of waves caused by these perturbations. Assuming that the waves come from the directions θ_1 and θ_2, the corresponding pattern of solid fraction is described by

$$p(v') = \mathrm{Re}\{v_e[\exp(\mathrm{i}K_{\theta 1}L_{\theta 1}) + \exp(\mathrm{i}K_{\theta 2}L_{\theta 2})]\}. \tag{21}$$

For example, two perpendicular perturbations such as shown in figure 23(*a*) cause the formation of square patterns like those in figure 23(*b*). If three perturbations with equal inclinations act on the base state, a kind of hexagon pattern as shown in figure 24 will occur at the surface.

Here these are three selection mechanisms in determining the patterns. The first is wavenumber selection, which has been solved in this model: only a perturbation

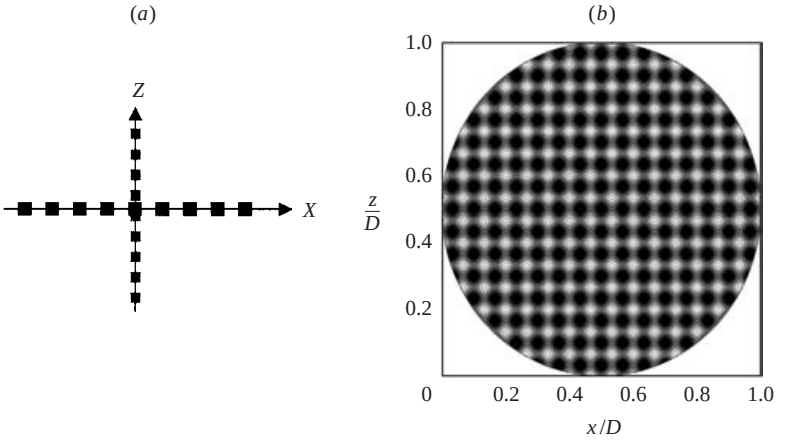

FIGURE 23. Pattern of squares: (*a*) two perpendicular perturbations; (*b*) squares from simulation, $(M_t,\ Q_t) = (4.75, 51.31)$, $K_x = 2.2$.

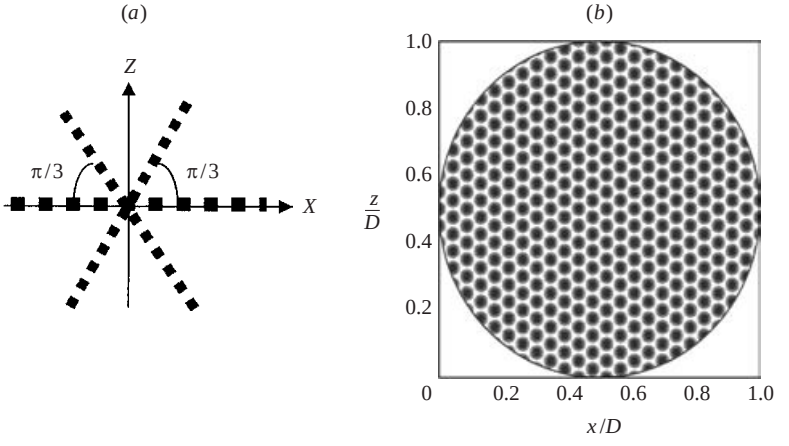

FIGURE 24. Pattern of hexagons: (*a*) three perturbations with equal inclinations; (*b*) hexagons from simulation, $(M_t,\ Q_t) = (4.75, 51.31)$, $K_x = 2.2$.

with a certain wavenumber will be dominant for a base state. The second is pattern selection: only specific patterns are favoured. For example, squares but not rhombi can be observed although the inclination between two perturbations may be of any possible angle. Unfortunately, similar to the problem faced by Tsimring & Aranson (1997), the present model is insensitive to the angle between two standing waves. The third is regime selection: the stripes, squares, hexagons and other patterns only appear in a special range of operating conditions. This may be found by examining the energy consumption with the nonlinear analysis and its effect on the long-term behaviour of the patterns formation.

A study of other eigenvectors than solid fraction can be helpful in providing insight into the evolution of the patterns predicted by the linear stability analysis. The following discussion concentrates on the standing waves occurring at point B. From the simulation results, the eigenvector of U_e is always found to be a pure imaginary number when $\Omega_i = 0$ and cannot produce visible velocity in the horizontal direction; thus it is not important in the consideration of standing waves.

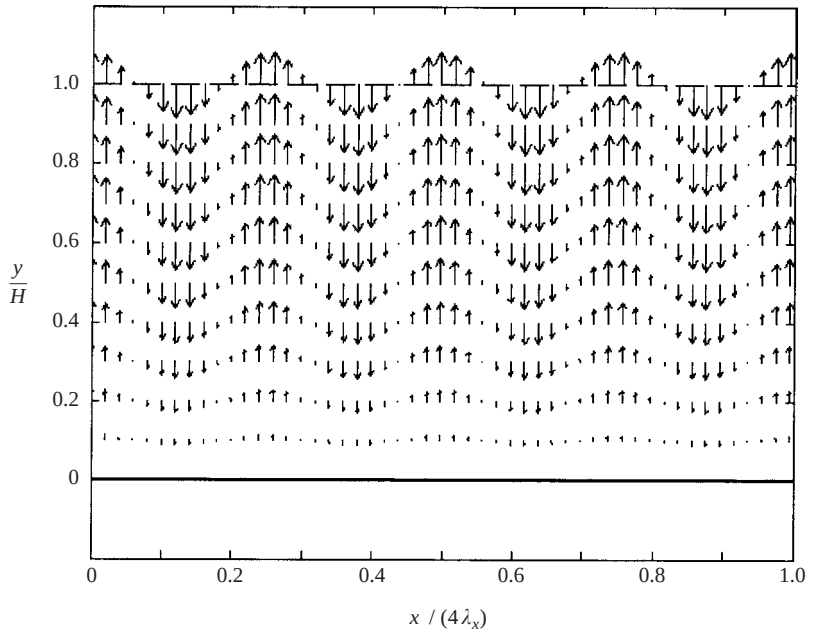

FIGURE 25. Vertical velocity distribution in the layer of granular material, $(M_t,\ Q_t) = (4.75,\ 51.31)$, $K_x = 2.2$.

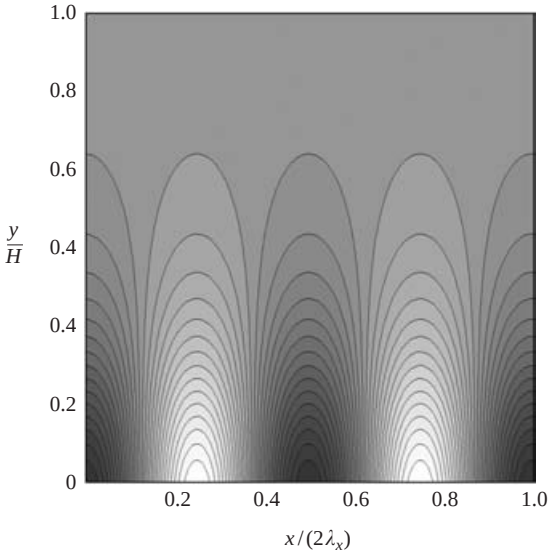

FIGURE 26. Profile of particle temperature in the (X, Y)-plane, $(M_t,\ Q_t) = (4.75,\ 51.31)$, $K_x = 2.2$.

As stated above, V_e increases from zero at the bottom plate to a peak at the top surface. Therefore, the granular layers no longer remain static under the perturbation but move towards their locations in the new stable base state (as a standing wave) with non-zero finite velocities. As shown in figure 25, particles may move upwards or downwards in different areas. The free surface does not remain flat, but peaks and

valleys will form which finally evolve into stable wave patterns such as squares and stripes.

Figure 26 shows the profile of T_e in the (X, Y)-plane. It is periodic in the X-direction and increases or decreases monotonically in the Y-direction. Thus, severe non-uniformity in the distribution of granular temperature is expected in the new base state to be formed.

By comparing with the ν_e profile shown in figure 15, we can illustrate the formation of patterns. At the beginning, the perturbations of velocity, solid fraction and particle temperature are very small in magnitude. As time passes, they begin to grow: in some regions, the solid fraction becomes denser, particles move downwards and the particle temperature increases; in other regions, the opposite changes occur at the same time. This finally leads to a stable new base state with an uneven surface, while the detailed evolution can be traced with the nonlinear stability analysis.

7. Conclusions

A simple assembly of granular material that is vertically vibrated exhibits many and surprising behaviours. The model adopted here can examine many aspects of the system such as base-state solutions, the stability diagram, and vertical and surface patterns. Although, further improvement of model is required, such as constructing a dispersion relation at high vibration frequencies and providing principles for pattern and regime selections, this model provides insight into the instabilities of the whole bed instead of only the surface patterns. Examination of the long-term behaviour of the patterns predicted by the linear stability analysis is currently underway and may offer a better understanding of the transition from one unstable state to new stable base state.

This project is supported by National University of Singapore under the grant R-279-000-095-112 and Singapore-MIT Alliance under the grant C382-429-003-091. The authors thank Professor Kenneth A. Smith (MIT) for his valuable advice on the patterns exploration. We also thank Dr. Jingsong Hua for his valuable suggestion on the base state study and Dr. Madhusudana Rao Suryadevara for his help in the preparation of this manuscript.

Appendix A. Linearized equations under the action of small perturbations

The equations of motion under the action of small perturbations can finally be linearized as

$$\frac{\partial \nu'}{\partial \tau} + \nu_0 \frac{\partial U'}{\partial X} + \nu_0 \frac{\partial V'}{\partial Y} + \frac{\partial \nu_0}{\partial Y} V' = 0, \tag{A 1}$$

$$\begin{aligned} &-\frac{1}{C}\nu_0 \frac{\partial U'}{\partial \tau} + C^{1/2} \frac{\partial}{\partial Y}\left[f_2(\nu_0) T_0^{1/2}\right] \frac{\partial U'}{\partial Y} + C^{1/2} \frac{\partial}{\partial Y}\left[f_2(\nu_0) T_0^{1/2}\right] \frac{\partial V'}{\partial X} - T_0 \frac{\partial f_1}{\partial \nu}\bigg|_{\nu_0} \frac{\partial \nu'}{\partial X} \\ &- f_1(\nu_0) \frac{\partial T'}{\partial X} + \left[C^{1/2} f_9(\nu_0) T_0^{1/2} + \tfrac{4}{3} C^{1/2} f_2(\nu_0) T_0^{1/2}\right] \frac{\partial^2 U'}{\partial X^2} + C^{1/2} f_2(\nu_0) T_0^{1/2} \frac{\partial^2 U'}{\partial Y^2} \\ &+ \left[C^{1/2} f_9(\nu_0) T_0^{1/2} + \tfrac{1}{3} C^{1/2} f_2(\nu_0) T_0^{1/2}\right] \frac{\partial^2 V'}{\partial X \partial Y} = 0, \end{aligned} \tag{A 2}$$

$$-\frac{1}{C}\nu_0\frac{\partial V'}{\partial\tau}+\left[-\frac{1}{C}-\frac{\partial}{\partial Y}\left(T_0\frac{\partial f_1}{\partial\nu}\bigg|\nu_0\right)\right]\nu'-\frac{\partial f_1}{\partial Y}\bigg|\nu_0 T'+\left\{C^{1/2}\frac{\partial}{\partial Y}\left[f_9(\nu_0)T_0^{1/2}\right]\right.$$
$$\left.-\tfrac{2}{3}C^{1/2}\frac{\partial}{\partial Y}\left[f_2(\nu_0)T_0^{1/2}\right]\right\}\frac{\partial U'}{\partial X}+\left\{C^{1/2}\frac{\partial}{\partial Y}\left[f_9(\nu_0)T_0^{1/2}\right]+\tfrac{4}{3}C^{1/2}\frac{\partial}{\partial Y}\left[f_2(\nu_0)T_0^{1/2}\right]\right\}\frac{\partial V'}{\partial Y}$$
$$-T_0\frac{\partial f_1}{\partial\nu}\bigg|\nu_0\frac{\partial\nu'}{\partial Y}-f_1(\nu_0)\frac{\partial T'}{\partial Y}+\left[C^{1/2}f_9(\nu_0)T_0^{1/2}+\tfrac{1}{3}C^{1/2}f_2(\nu_0)T_0^{1/2}\right]\frac{\partial^2 U'}{\partial X\partial Y}$$
$$+C^{1/2}f_2(\nu_0)T_0^{1/2}\frac{\partial^2 V'}{\partial X^2}+\left[C^{1/2}f_9(\nu_0)T_0^{1/2}+\tfrac{4}{3}C^{1/2}f_2(\nu_0)T_0^{1/2}\right]\frac{\partial^2 V'}{\partial Y^2}=0, \tag{A 3}$$

$$-\frac{3\nu_0}{2C^{3/2}}\frac{\partial T'}{\partial\tau}-\frac{3\nu_0}{2C^{3/2}}\frac{\partial T_0}{\partial Y}V'+\left\{\frac{\partial}{\partial Y}\left[T_0^{1/2}\frac{\partial f_3}{\partial\nu}\bigg|\nu_0\frac{\partial T_0}{\partial Y}\right]+\frac{\partial}{\partial Y}\left[T_0^{3/2}\frac{\partial f_4}{\partial\nu}\bigg|\nu_0\frac{\partial\nu_0}{\partial Y}\right]\right.$$
$$-\frac{1}{C^2}T_0^{3/2}\frac{\partial f_5}{\partial\nu}\bigg|\nu_0\Big\}\nu'+\left\{\frac{\partial}{\partial Y}\left[\tfrac{1}{2}f_3(\nu_0)T_0^{-1/2}\frac{\partial T_0}{\partial Y}\right]+\frac{\partial}{\partial Y}\left[\tfrac{3}{2}f_4(\nu_0)T_0^{1/2}\frac{\partial\nu_0}{\partial Y}\right]\right.$$
$$\left.-\frac{3}{2}\frac{1}{C^2}f_5(\nu_0)T_0^{1/2}\right\}T'-C^{-3/2}f_1(\nu_0)T_0\frac{\partial U'}{\partial X}-C^{-3/2}f_1(\nu_0)T_0\frac{\partial V'}{\partial Y}+\left\{T_0^{3/2}\frac{\partial f_4}{\partial\nu}\bigg|\nu_0\frac{\partial\nu_0}{\partial Y}\right.$$
$$+\frac{\partial}{\partial Y}\left[f_4(\nu_0)T_0^{3/2}\right]+T_0^{1/2}\frac{\partial f_3}{\partial\nu}\bigg|\nu_0\frac{\partial T_0}{\partial Y}\Big\}\frac{\partial\nu'}{\partial Y}+\left\{\tfrac{1}{2}f_3(\nu_0)T_0^{-1/2}\frac{\partial T_0}{\partial Y}+\tfrac{3}{2}f_4(\nu_0)T_0^{1/2}\frac{\partial\nu_0}{\partial Y}\right.$$
$$\left.+\frac{\partial}{\partial Y}\left[f_3(\nu_0)T_0^{1/2}\right]\right\}\frac{\partial T'}{\partial Y}+f_4(\nu_0)T_0^{3/2}\frac{\partial^2\nu'}{\partial X^2}+f_4(\nu_0)T_0^{3/2}\frac{\partial^2\nu'}{\partial Y^2}$$
$$+f_3(\nu_0)T_0^{1/2}\frac{\partial^2 T'}{\partial X^2}+f_3(\nu_0)T_0^{1/2}\frac{\partial^2 T'}{\partial Y^2}=0. \tag{A 4}$$

Here (A 1) is the continuity equation, (A 2) and (A 3) are the two components of the momentum balance, and (A 4) represents the balance of pseudo-thermal energy.

The corresponding boundary conditions at $Y=0$ are

$$\frac{f_8(\nu_0)}{C}\phi' U'-\frac{\partial U'}{\partial Y}-\frac{\partial V'}{\partial X}=0, \tag{A 5}$$
$$V'=0, \tag{A 6}$$

$$\left\{T_0^{1/2}\frac{\partial f_3}{\partial\nu}\bigg|\nu_0\frac{\partial T_0}{\partial Y}+T_0^{3/2}\frac{\partial f_4}{\partial\nu}\bigg|\nu_0\frac{\partial\nu_0}{\partial Y}-\frac{1-e_w^2}{C}f_3(\nu_0)T_0^{3/2}\frac{\partial f_6}{\partial\nu}\bigg|\nu_0\right.$$
$$-\frac{1-e_w^2}{C}f_6(\nu_0)T_0^{3/2}\frac{\partial f_3}{\partial\nu}\bigg|\nu_0\Big\}\nu'+\left\{\tfrac{1}{2}f_3(\nu_0)T_0^{-1/2}\frac{\partial T_0}{\partial Y}+\tfrac{3}{2}f_4(\nu_0)T_0^{1/2}\frac{\partial\nu_0}{\partial Y}\right.$$
$$\left.-\frac{1-e_w^2}{C}f_3(\nu_0)f_6(\nu_0)\tfrac{3}{2}T_0^{1/2}\right\}T'+f_4(\nu_0)T_0^{3/2}\frac{\partial\nu'}{\partial Y}+f_3(\nu_0)T_0^{1/2}\frac{\partial T'}{\partial Y}=0, \tag{A 7}$$

and those at $Y=1$ are

$$\left(T_0\frac{\partial f_1}{\partial\nu}\bigg|\nu_0-\frac{\pi}{9}\frac{\nu^{-1/3}}{\nu_m^{2/3}}\right)\nu'+f_1(\nu_0)T'+\left[\tfrac{2}{3}f_2(\nu_0)T_0^{1/2}C^{1/2}-f_9(\nu_0)T_0^{1/2}C^{1/2}\right]\frac{\partial U'}{\partial X}$$
$$+\left[-f_9(\nu_0)T_0^{1/2}C^{1/2}-\tfrac{4}{3}f_2(\nu_0)T_0^{1/2}C^{1/2}\right]\frac{\partial V'}{\partial Y}=0, \tag{A 8}$$

	n	10	30	50	70	100
	Δ	0.1	0.0333	0.02	0.0143	0.01
	H (10^{-2} m)	0.44016	0.43229	0.43166	0.43146	0.43137
ν_0	$Y = 0$	0.16762	0.16905	0.1693	0.1692	0.16921
	$Y = 0.2$	0.24738	0.2494	0.25	0.24972	0.24973
	$Y = 0.4$	0.33773	0.34174	0.34248	0.34217	0.3422
	$Y = 0.6$	0.41033	0.4165	0.41747	0.41718	0.41725
	$Y = 0.8$	0.43415	0.44243	0.44366	0.44343	0.44354
	$Y = 1.0$	0.35048	0.36049	0.3621	0.36198	0.36216
T_0^*	$Y = 0$	7.21457	7.11055	7.09243	7.10043	7.09963
	$Y = 0.2$	2.71386	2.66821	2.65923	2.66401	2.66375
	$Y = 0.4$	0.96097	0.93267	0.92812	0.92998	0.92976
	$Y = 0.6$	0.36451	0.34787	0.34552	0.34619	0.34603
	$Y = 0.8$	0.17094	0.16041	0.15899	0.15924	0.15912
	$Y = 1.0$	0.1203	0.11204	0.11075	0.11085	0.11071

TABLE 3. Base-state solutions for different grid sizes. Point A, $(M_t,\ Q_t) = (3.0,\ 19.83)$.

	n	10	30	50	70	100
	Δ	0.1	0.0333	0.02	0.0143	0.01
	H (10^{-2} m)	0.59128	0.57682	0.57565	0.57545	0.57526
ν_0	$Y = 0$	0.13377	0.135	0.13501	0.1353	0.13525
	$Y = 0.2$	0.23849	0.24076	0.24077	0.24128	0.24118
	$Y = 0.4$	0.38141	0.3895	0.38984	0.39072	0.39065
	$Y = 0.6$	0.50243	0.51415	0.51491	0.51574	0.51574
	$Y = 0.8$	0.55535	0.5683	0.56927	0.57002	0.57007
	$Y = 1.0$	0.49146	0.51297	0.51516	0.51656	0.51681
T_0^*	$Y = 0$	17.19057	16.95006	16.94869	16.91084	16.91722
	$Y = 0.2$	4.71812	4.63447	4.63666	4.61768	4.62143
	$Y = 0.4$	1.05493	0.9882	0.98504	0.97865	0.97915
	$Y = 0.6$	0.24144	0.21384	0.21215	0.21031	0.2103
	$Y = 0.8$	0.07175	0.05998	0.05917	0.05852	0.05847
	$y = 1.0$	0.03982	0.03235	0.03164	0.03119	0.03111

TABLE 4. Base-state solutions for different grid sizes. Point B, $(M_t,\ Q_t) = (4.75,\ 51.31)$.

$$\frac{\partial U'}{\partial Y} + \frac{\partial V'}{\partial X} = 0, \tag{A 9}$$

$$\left[T_0^{1/2}\frac{\partial f_3}{\partial \nu}\bigg|\nu_0\frac{\partial T_0}{\partial Y} + T_0^{3/2}\frac{\partial f_4}{\partial \nu}\bigg|\nu_0\frac{\partial \nu_0}{\partial Y}\right]\nu' + \left[\tfrac{1}{2}f_3(\nu_0)T_0^{-1/2}\frac{\partial T_0}{\partial Y} + \tfrac{3}{2}f_4(\nu_0)T_0^{1/2}\frac{\partial \nu_0}{\partial Y}\right]T'$$
$$+ f_4(\nu_0)T_0^{3/2}\frac{\partial \nu'}{\partial Y} + f_3(\nu_0)T_0^{1/2}\frac{\partial T'}{\partial Y} = 0. \tag{A 10}$$

Appendix B. Spatial resolution in the numerical methods

The determination of grid size Δ (or the number of the grid points, n) is important for the calculation of both the base-state solutions and eigenvalues. If Δ is too large, the results are grid-size-dependent; if it is too small, the calculation time is too long and there is the problem of rounding error accumulation. Therefore, a moderate grid size is sought to obtain the accurate results.

K_x	n	Δ	Ω_r	$\lvert\Omega_i\rvert$
0	50	0.02	0.00161	0
	100	0.01	0.00234	0
	150	0.0067	0.00252	0
	200	0.005	0.00260	0
	250	0.004	0.00263	0
	300	0.0033	0.00265	0
0.5	50	0.02	−0.12439	0.07187
	100	0.01	−0.12401	0.07408
	150	0.0067	−0.12392	0.07457
	200	0.005	−0.12389	0.07475
	250	0.004	−0.12387	0.07484
	300	0.0033	−0.12386	0.07488

TABLE 5. Eigenvalues obtained at different grid sizes. Point A, $(M_t, Q_t) = (3.0, 19.83)$.

K_x	n	Δ	Ω_r	$\lvert\Omega_i\rvert$
1.0	50	0.02	−0.22632	0.07163
	100	0.01	−0.22886	0.07582
	150	0.0067	−0.22917	0.07699
	200	0.005	−0.22926	0.07747
	250	0.004	−0.22930	0.07771
	300	0.0033	−0.22932	0.07784
2.2	50	0.02	0.01618	0
	100	0.01	0.00516	0
	150	0.0067	0.00291	0
	200	0.005	0.00209	0
	250	0.004	0.00169	0
	300	0.0033	0.00148	0

TABLE 6. Eigenvalues obtained at different grid sizes. Point B, $(M_t, Q_t) = (4.75, 51.31)$.

Table 3 and table 4 list the bed height H, solid fraction ν_0 and dimensionless granular temperature T_0^* calculated from the base-state solution at different grid sizes for point A and point B, respectively. It can be seen that the solutions vary little from $n = 70$ to $n = 100$. Thus, a grid size of 0.01 is chosen for the base-state calculation.

Table 5 and table 6 list the eigenvalues (including real part Ω_r and imaginary part Ω_i) calculated for different grid sizes in the stability analysis for points A and B, respectively. Based on these results, a grid size of 0.005 is selected for the stability analysis.

REFERENCES

AOKI, K. M. & AKIYAMA, T. 1996 Spontaneous wave pattern formation in vibrated granular materials. *Phys. Rev. Lett.* **77**, 4166–4169.

BIZON, C., SHATTUCK, M. D. & SWIFT, J. B. 1999 Linear stability analysis of a vertically oscillated granular layer. *Phys. Rev.* E **60**, 7210–7216.

BIZON, C., SHATTUCK, M. D., SWIFT, J. B., MCCORMICK, W. D. & SWINNEY, H. L. 1998*a* Patterns in 3D vertically oscillated granular layers: simulation and experiment. *Phys. Rev. Lett.* **80**, 57–60.

Bizon, C., Shattuck, M. D., deBruyn, J. R., Swift, J. B., McCormick, W. D. & Swinney, H. L. 1998*b* Convection and diffusion in vertically vibrated granular patterns. *J. Statist Phys.* **93**, 449–465.

Brennen, C. E., Ghosh, S. & Wassgren, C. R. 1996 Vertical oscillation of a bed of granular material. *J. Appl. Mech.* **63**, 156–161.

Clement, E., Vanel, L., Rajchenbach, J. & Duran, J. 1996 Pattern formation in a vibrated granular layer. *Phys. Rev.* E **53**, 2972–2976.

Hunt, M. L., Hsiau, S. & Hong, K. T. 1994 Particle mixing and volumetric expansion in a vibrated granular bed. *Trans. ASME: J. Fluids Engng* **116**, 785.

Johnson, P. C. & Jackson, R. 1987 Frictional-collisional constitutive relations for granular materials, with application to plane shearing. *J. Fluid Mech.* **176**, 67–93.

Kadanoff, L. P. 1999 Built upon sand: Theoretical ideas inspired by granular flows. *Rev. Mod. Phys.* **71**, 435–444.

Lan, Y. & Rosato, A. D. 1995 Macroscopic behavior of vibrating beds of smooth inelastic spheres. *Phys. Fluids* **7**, 1818–1832.

Luding, S., Clement, E., Blumen, A., Rajchenbach, J. & Duran, J. 1994 Studies of columns of beads under external vibrations. *Phys. Rev.* E **49**, 1634–1646.

Lun, C. K. K, Savage, S. B., Jeffrey, D. J. & Chepurniy, N. 1984 Kinetic theories for granular flow: Inelastic particles in Couette flow and slightly inelastic particles in a general flow field. *J. Fluid Mech.* **140**, 223–256.

Melo, F., Umbanhowar, P. B. & Swinney, H. L. 1994 Transition to parametric wave patterns in a vertically oscillated granular layers. *Phys. Rev. Lett.* **72**, 172–176.

Melo, F., Umbanhowar, P. B. & Swinney, H. L. 1995 Hexagons, kinks and disorder in oscillated granular layers. *Phys. Rev. Lett.* **75**, 3838–3841.

Metcalf, T. H., Knight, J. B. & Jaeger, H. M. 1997 Standing wave patterns in shallow beds of vibrated granular material. *Physica* A **236**, 202–210.

Pak, H. K & Behringer, R. P. 1993 Surface waves in vertically vibrated granular materials. *Phys. Rev. Lett.* **71**, 1832–1835.

Richman, M. W. & Martin, R. E. 1992 Unconfined granular materials thermalized by fluctuating horizontal surface. *Proc. 9th conf. on Engineering Mechanics* (ed. L. D. Lutes & J. M. Niedzwecki), pp. 901–903.

Shattuck, M. D., Bizon, C., Swift, J. N. & Swinney, H. L. 1999 Computational test of kinetic theory of granular media. *Physica* A **274**, 158–170.

Shinbrot, T. 1997 Competition between randomized impacts and inelastic collisions in granular pattern formation. *Nature* **389**, 574–576.

Tsimring, L. S. & Aranson, I. S. 1997 Localized and cellular patterns in a vibrated granular layer. *Phys. Rev. Lett.* **79**, 213–216.

Umbanhowar, P. B. 1997 Patterns in the sand. *Nature* **389**, 541–542.

Umbanhowar, P. B., Melo, F. & Swinney, H. L. 1996 Localized excitations in a vertically vibrated granular layer. *Nature* **382**, 793–796.

Umbanhowar, P. B., Melo, F. & Swinney, H. L. 1998 Periodic, aperiodic, and transient patterns in vibrated granular layers. *Physica* A **249**, 1–9.

Umbanhowar, P. B. & Swinney, H. L. 2000 Wavelength scaling and square/stripe and grain mobility transitions in vertically oscillated granular layers. *Physica* A **288**, 344–362.

Wang, C. H., Sundaresan, S. & Jackson, R. 1997 Instabilities of fully developed rapid flow of a granular material in a channel. *J. Fluid Mech.* **342**, 179–197.

Wang, C. H. & Tong, Z. 1998 Transient development of instabilities in bounded shear flow of granular materials. *Chem. Engng Sci.* **53**, 3803–3819.

Wang, C. H. & Tong, Z. 2001 On the density waves developed in gravity channel flows of granular materials. *J. Fluid Mech.* **435**, 217–246.

Wildman, R. D., Huntley, J. M. & Parker, D. J. 2001*a* Granular temperature profiles in three-dimensional vibrofluidized granular beds. *Phys. Rev.* E **63**, 061311:1–10.

Wildman, R. D., Huntley, J. M. & Parker, D. J. 2001*b* Convection in highly fluidized three-dimensional granular beds. *Phys. Rev. Lett.* **86**, 3304–3307.

Yang, X., Huan, C., Candela, D., Mair, R. W. & Walsworth, R. L. 2002 Measurements of grain motion in a dense, three-dimensional granular fluid. *Phys. Rev. Lett.* **88**, 044301:1–4.